Cell Reports

Article

Vaccine-associated enhanced respiratory pathology in COVID-19 hamsters after T_H2-biased immunization

Graphical abstract

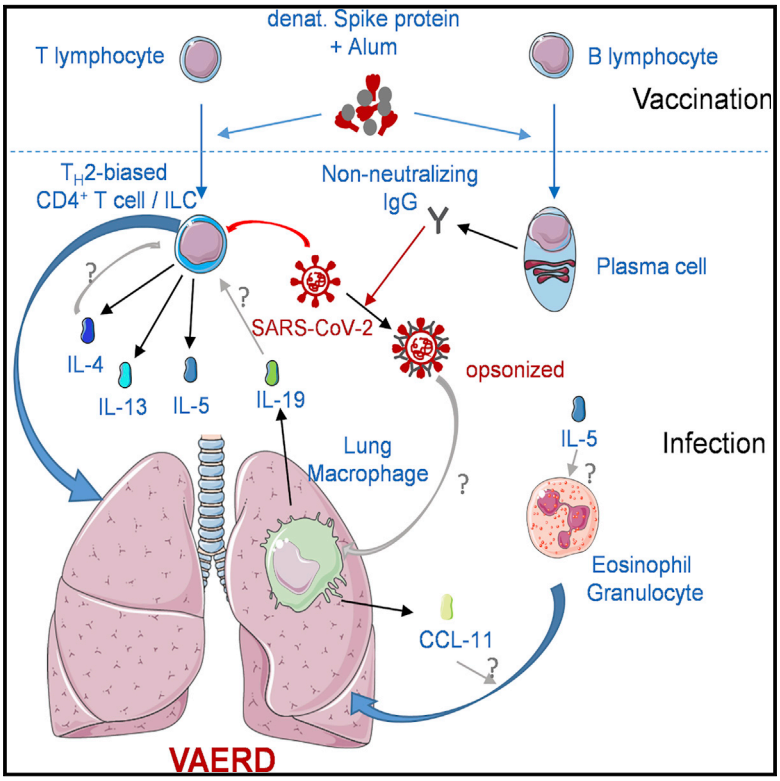

Highlights

- T_H2-biased vaccines can prime immunopathogenesis in Syrian hamsters with COVID-19
- VAERD correlates with T_H2 cytokines and non-neutralizing antibodies
- T cells, innate lymphoid cells, and lung macrophages are dysregulated in VAERD
- VAERD can be treated with dexamethasone

Authors

Aileen Ebenig, Samada Muraleedharan, Julia Kazmierski, ..., Christine Goffinet, Richard J.P. Brown, Michael D. Mühlebach

Correspondence

michael.muehlebach@pei.de

In brief

Ebenig et al. report vaccine-associated enhanced respiratory disease (VAERD) in SARS-CoV-2-infected Syrian hamsters previously immunized with a suboptimal vaccine consisting of misfolded SARS-CoV-2 spike protein and Alum adjuvants. VAERD is correlated with dysregulation of specific immune cell subsets in the lungs and could be alleviated by dexamethasone treatment.

Ebenig et al., 2022, Cell Reports *40*, 111214
August 16, 2022 © 2022 The Author(s).
https://doi.org/10.1016/j.celrep.2022.111214

CellPress

Cell Reports

CellPress
OPEN ACCESS

Article

Vaccine-associated enhanced respiratory pathology in COVID-19 hamsters after T_H2-biased immunization

Aileen Ebenig,[1] Samada Muraleedharan,[1] Julia Kazmierski,[2] Daniel Todt,[3,4] Arne Auste,[1,5] Martina Anzaghe,[6] André Gömer,[3,7] Dylan Postmus,[2] Patricia Gogesch,[6] Marc Niles,[6] Roland Plesker,[8] Csaba Miskey,[9] Michelle Gellhorn Serra,[10] Angele Breithaupt,[11] Cindy Hörner,[1,5] Carina Kruip,[1] Rosina Ehmann,[12] Zoltan Ivics,[9] Zoe Waibler,[6] Stephanie Pfaender,[3] Emanuel Wyler,[13] Markus Landthaler,[13,14] Alexandra Kupke,[5,10] Geraldine Nouailles,[15,16] Christine Goffinet,[2] Richard J.P. Brown,[17] and Michael D. Mühlebach[1,5,18,*]

[1]Product Testing of IVMPs, Div. of Veterinary Medicines, Paul-Ehrlich-Institut, 63225 Langen, Germany
[2]Institute of Virology, Campus Charité Mitte, Charité - Universitätsmedizin Berlin, Corporate Member of Freie Universität Berlin and Humboldt-Universität zu Berlin, 10117 Berlin, Germany
[3]Department for Molecular and Medical Virology, Ruhr-University, 44801 Bochum, Germany
[4]European Virus Bioinformatics Center (EVBC), 07743 Jena, Germany
[5]German Center for Infection Research, Gießen-Marburg-Langen, Germany
[6]Div. of Immunology, Paul-Ehrlich-Institut, 63225 Langen, Germany
[7]Institute of Virology, University of Veterinary Medicine Hannover, 30559 Hannover, Germany
[8]Animal Facilities, Div. Veterinary Medicines, Paul-Ehrlich-Institut, 63225 Langen, Germany
[9]Div. of Medical Biotechnology, Paul-Ehrlich-Institut, 63225 Langen, Germany
[10]Institute for Virology, Phillipps-University, 35043 Marburg, Germany
[11]Department of Experimental Animal Facilities and Biorisk Management, Friedrich-Loeffler-Institut, Federal Research Institute for Animal Health, 17493 Greifswald-Insel Riems, Germany
[12]Institute for Microbiology, Bundeswehr, 80937 München, Germany
[13]Berlin Institute for Medical Systems Biology (BIMSB), Max Delbrück Center for Molecular Medicine in the Helmholtz Association (MDC), 10115 Berlin, Germany
[14]IRI Life Sciences, Institute for Biology, Humboldt-Universität zu Berlin, 10115 Berlin, Germany
[15]Division of Pulmonary Inflammation, Charité - Universitätsmedizin Berlin, Corporate Member of Freie Universität Berlin and Humboldt-Universität zu Berlin, 10117 Berlin, Germany
[16]Department of Infectious Diseases and Respiratory Medicine, Charité - Universitätsmedizin Berlin, Corporate Member of Freie Universität Berlin and Humboldt-Universität zu Berlin, 10117 Berlin, Germany
[17]Virus Tropism and Immunogenicity, Div. of Veterinary Medicine, Paul-Ehrlich-Institut, 63225 Langen, Germany
[18]Lead contact
*Correspondence: michael.muehlebach@pei.de
https://doi.org/10.1016/j.celrep.2022.111214

SUMMARY

Vaccine-associated enhanced respiratory disease (VAERD) is a severe complication for some respiratory infections. To investigate the potential for VAERD induction in coronavirus disease 2019 (COVID-19), we evaluate two vaccine leads utilizing a severe hamster infection model: a T helper type 1 (T_H1)-biased measles vaccine-derived candidate and a T_H2-biased alum-adjuvanted, non-stabilized spike protein. The measles virus (MeV)-derived vaccine protects the animals, but the protein lead induces VAERD, which can be alleviated by dexamethasone treatment. Bulk transcriptomic analysis reveals that our protein vaccine prepares enhanced host gene dysregulation in the lung, exclusively up-regulating mRNAs encoding the eosinophil attractant CCL-11, T_H2-driving interleukin (IL)-19, or T_H2 cytokines IL-4, IL-5, and IL-13. Single-cell RNA sequencing (scRNA-seq) identifies lung macrophages or lymphoid cells as sources, respectively. Our findings imply that VAERD is caused by the concerted action of hyperstimulated macrophages and T_H2 cytokine-secreting lymphoid cells and potentially links VAERD to antibody-dependent enhancement (ADE). In summary, we identify the cytokine drivers and cellular contributors that mediate VAERD after T_H2-biased vaccination.

INTRODUCTION

Severe acute respiratory syndrome coronavirus 2 (SARS-CoV-2) is the etiological agent of the current coronavirus disease 2019 (COVID-19) pandemic (Wu et al., 2020; Zhu et al., 2020), resulting in more than 513 million confirmed cases (as of May 5, 2022) with an overall case fatality rate of 1.21% (WHO, 2021). To combat this pandemic, the first vaccine candidates were developed, tested in animal models, and approved for human use within the first year after pathogen identification. To date, more than 10 billion vaccine doses have been administered of all authorized vaccines based on different vaccine technologies, namely

This is an open access article under the CC BY license (http://creativecommons.org/licenses/by/4.0/).

mRNA vaccines, adenoviral vector vaccines, inactivated viruses, or proteins. Potential safety risks including the induction of a more severe or altered clinical pathology after breakthrough infection in vaccinated patients were considered, but not yet described, during their development.

One possible risk associated with immunization in the context of respiratory infections is an immunopathology termed vaccine-associated enhanced respiratory disease (VAERD) (Munoz et al., 2021). Such enhancement of disease has been well described in the context of formalin-inactivated respiratory syncytial virus (RSV) vaccines for infants and young children (Kim et al., 1969). Vaccinated children who were later exposed to circulating RSV developed an enhanced and atypical phenotype of clinical symptoms that resulted in higher hospitalization rates and even a small number of associated fatalities (Kim et al., 1969). Lung sections of the fatal cases displayed monocytic infiltration with massive excess of eosinophils (Kim et al., 1969). Induction of low-affinity and non-neutralizing antibody (Ab) responses provoked by the formalin-inactivated virus was found to be causative for enhanced disease (Polack et al., 2002). Such a pathologic eosinophil infiltration triggered by T_H2-biased T cell responses has also been demonstrated in animal models after immunization with formalin-inactivated virus prior to RSV infection (Ruckwardt et al., 2019).

Immunopathologies such as VAERD or Ab-dependent enhancement (ADE) of disease were also reported in CoV-infected vaccinated animals or animal models for highly pathogenic human CoV. Cats immunized with a recombinant S protein-expressing vaccinia virus developed more severe disease and early death syndrome following infection with feline infectious peritonitis virus, which was linked to a low amount of vaccine-induced neutralizing Abs in the affected animals (Vennema et al., 1990). Passive transfer of Abs directed against the virus before infection was sufficient for pathology, which was correlated to accelerated virus uptake by macrophages via Fc receptor (Olsen et al., 1992; Takano et al., 2008). Such processes are considered a marker and relevant for classical ADE as described for dengue virus (DENV) (Beltramello et al., 2010). Also, animal models for the first two highly pathogenic zoonotic beta-CoVs, SARS-CoV and Middle Eastern respiratory syndrome (MERS)-CoV, revealed potential for VAERD. Entry receptor-transgenic K18-ACE2 or hDPP4 mice that were immunized with whole inactivated virus vaccines developed severe immunopathology in lung tissue with infiltration of eosinophils after infection (Bolles et al., 2011; Tseng et al., 2012; Agrawal et al., 2016).

These scenarios prompted careful evaluation of the predisposition of COVID-19 infection for disease enhancement. Induction of T_H2-biased immunity or non-functional Ab responses by the different front-runner vaccine candidates was avoided (Corbett et al., 2020a, 2020b; Ramasamy et al., 2020; Sahin et al., 2020; Sadoff et al., 2021; van der Lubbe et al., 2021). Accordingly, no ERD or ADE has been reported in vaccinated individuals to date. However, two recent publications described evidence for VAERD in per se T_H2-biased mouse models using mouse-adapted recombinant SARS-CoV-2 after immunization with alum-adjuvanted, whole-inactivated SARS-CoV-2 or adjuvanted S protein. Following virus challenge, these animals developed considerable pneumonia with infiltration of eosinophils and neutrophils, a clear sign of VAERD (DiPiazza et al., 2021; Iwata-Yoshikawa et al., 2022). Again, the pathology was linked to induction of cytokines typical for T_H2-biased immune responses, but no detailed mechanism for the pathogenesis was described.

We have previously shown in the Syrian hamster (*Mesocricetus auratus*) COVID-19 model that alum-adjuvanted spike protein failed to protect against severe disease after infection, in contrast to a measles vaccine-derived prototypic COVID-19 vaccine (Hörner et al., 2020). Here, we report reproducible VAERD in outbred hamsters with no inbred helper cell bias. Those hamsters were vaccinated with alum-adjuvanted S protein and later infected with a low-passage human patient isolate. This model allowed us to identify the mechanisms that underlie the observed immunopathology. VAERD became evident in the respective hamsters' lungs: ISH, immunohistochemistry, staining for eosinophils, and general histopathology revealed exaggeration of pneumonia and eosinophilic infiltration, while virus load was reduced. These effects could be correlated to a broadly enhanced dysregulation of gene expression: up-regulation of the major eosinophil attractant eotaxin-1/CCL-11 combined with induction of T_H2-marker cytokines interleukin (IL)-4, IL-5, and IL-13 supported by IL-19 was evident. Furthermore, using single-cell RNA sequencing (scRNA-seq), we attributed this dysregulation to specific immune cell subsets, suggesting that ADE via Fc-receptor-mediated skewing of virion uptake drives CCL-11 and IL-19 secretion by lung macrophages. These cytokines attract eosinophils and positively feedback on the T/NK cell compartment responsible for T_H2-marker cytokine secretion. Eosinophil infiltration and pathology observed in recombinant, non-stabilized SARS-CoV-2 S protein adjuvanted with aluminum hydroxide (Alum+S)-vaccinated animals were dramatically reduced by treatment of infected animals with dexamethasone, while the whole syndrome was absent in animals that received the T helper type 1 (T_H1)-biased measles virus (MeV)-derived vaccine candidate. These data allow us to propose a detailed model of vaccine-induced immunopathogenesis, involving immune cells of the lymphoid and myeloid compartment that release pro-inflammatory cytokines, in a gold-standard animal model of COVID-19. Our data also potentially link VAERD mechanistically to ADE, which will be the focus of follow-up studies.

RESULTS

Histological analysis and pulmonary virus load

To study the efficacy of MeV-derived COVID-19 vaccines, we vaccinated Syrian hamsters with the experimental vaccine candidate MeV_{vac2}-SARS2-S(H) and a classic protein vaccine formulation of recombinant, non-stabilized SARS-CoV-2 S protein adjuvanted with aluminum hydroxide (Alum+S). The recombinant S revealed distinct changes in secondary structural elements (31.7% α-helices and 35.0% β-sheets versus 19.3% α-helices and 50.8% β-sheets) compared with a stabilized soluble S (Figure S1), highlighting deviation (i.e., de-folding) of the vaccine protein from the native pre-fusion structure. Vaccinated animals were challenged in parallel to naive or vector-control hamsters (MV_{vac2}-ATU(P)) using the low-passage SARS-CoV-2 patient isolate BavPat1 (Hörner et al., 2020) (Figure 1A). During

histological analysis of lung necropsies, the expected pathology was observed for the control animals in hematoxylin and eosin (H&E)-stained tissue slices of the lungs (Figure 1B). In both naive and vector control hamsters, epithelia and endothelia in bronchii and vasculature, respectively, showed inflammation and hemorrhages. Between 20% and 80% (median 40%) of the lung area had become dense due to cellular infiltrates of macrophages and lymphocytes; in general, no or few eosinophils or granulocytes were observed. Single foci to moderate karyorrhexis were apparent (Table S1). This pathology was significantly ameliorated in MeV_{vac2}-SARS2-S(H)-vaccinated hamsters, with reduced inflammation (median of 27.5% dense area), very few hemorrhages, only a few eosinophils in perivascular regions, and no to minimal karyorrhexis. In contrast, animals vaccinated with Alum+S displayed a considerably intensified pathogenesis: while bronchial epithelia showed few inflammatory alterations, vascular endothelium revealed explicit inflammation. The area of dense infiltrates exceeded 50% of the slices, with massive infiltration of eosinophils (Figures 1B and 1D). Together, this histopathology suggests induction of VAERD by the immunization of hamsters with Alum+S.

Active SARS-CoV-2 infection became evident by *in situ* hybridization (ISH) of SARS-CoV-2 RNA genomes (Figures 1B, third row, and 1C) and immunohistochemistry for SARS-CoV-2 nucleocapsid protein N (Figure 1B, fourth row). MeV_{vac2}-SARS2-S(H)-vaccinated animals revealed significantly reduced staining for SARS-CoV-2 in both ISH and immunohistochemistry. These data are consistent with the previously published protective efficacy of this T_H1-biased vaccine concept. Additionally, Alum+S-vaccinated animals showed somewhat reduced staining for SARS-CoV-2 genomes and N, despite enhanced pathology. While up to 20% of the lung tissue stained positive for SARS-CoV-2 genomes in control animals, a maximum of only 5% did in hamsters vaccinated with MeV_{vac2}-SARS2-S(H), while Alum+S-vaccinated animals showed a split behavior (Figure 1C). Sirius red staining for eosinophils (Figure 1B, bottom row) validated H&E findings for significantly enhanced infiltration, which became evident to this extent only in this vaccine cohort. Only in 3 out of 6 animals vaccinated with MeV_{vac2}-SARS2-S(H) were some eosinophils found in perivascular regions of inflamed tissue (Figure S2). Between 84 and 155 eosinophils/mm^2 were found in lung sections of hamsters immunized with Alum+S, whereas in hamsters inoculated with MeV_{vac2}-SARS2-S(H), or the MeV vector control, eosinophil numbers remained within the same range as uninfected control hamsters (3–24 eosinophils/mm^2) (Figure 1D).

Thus, the COVID-19 hamster model revealed features suggestive of VAERD for animals vaccinated using the traditional T_H2-biased alum-adjuvanted protein vaccine approach but an absence of such an effect for the T_H1-biased measles-based COVID-19 vaccine candidate (Hörner et al., 2020).

Transcriptional profiling of SARS-CoV-2-infected hamster lungs

To identify determinants underlying the observed enhanced pathology, we performed RNA-seq profiling of hamster lung tissue. Lung transcriptomes from SARS-CoV-2-infected naive hamsters were compared with infected animals previously immunized with either T_H1- or T_H2-biased vaccines. Differentially expressed genes (DEGs) in lungs were determined by comparison with baseline expression levels, derived from uninfected, unvaccinated control animals. Principal component analysis (PCA) of individual transcriptomes revealed segregation of signals according to infection and vaccination status, confirming distinct lung transcriptional responses in the different groups (Figure 2A). Significant transcriptional dysregulation was evident in infected lung tissue, with ~2,000 genes down-regulated and ~1,500 genes up-regulated in vaccine-naïve, SARS-CoV-2-infected hamsters (Figure 2B, left panel). However, prior vaccination with MeV_{vac2}-SARS2-S(H) caused a 40% reduction in numbers of significantly dysregulated genes. In line with this, lung resident viral RNAs were also 20-fold reduced when compared with unvaccinated animals (Figure 2B, left panel). In contrast, challenge with SARS-CoV-2 after vaccination with Alum+S resulted in comparable numbers of dysregulated genes to those observed in unvaccinated animals (Figure 2B, left panel), with an increased median fold change in gene expression also apparent (Figure 2B, right panel). Only a 2-fold reduction in lung-resident viral RNAs was observed here (Figure 2B, left panel). Together, these data suggest that prior immunization with a T_H1-biased vaccine confers protection from disease, substantially reducing viral loads in hamster lungs, with a concomitant reduction in the magnitude of lung gene dysregulation. In contrast, the gene dysregulation and viral loads observed using the T_H2-biased vaccine more closely resembled patterns seen in unvaccinated animals. However, inspection of the PCA plot revealed separate clustering of unvaccinated and Alum+S groups (Figure 2A), indicating unique transcriptional signatures underlying Alum+S-associated pathology.

To investigate this in more detail, we performed Gene Ontology (GO) enrichment analyses to determine the associated biological processes (Figure 2C). In all groups, infection was associated with significant enrichment of genes associated with defense against pathogens and vigorous induction of classical antiviral and inflammatory response genes (Figure 2C, left panel). Of note, the magnitude of these responses was similar in unvaccinated and Alum+S-immunized hamsters and reduced in MeV_{vac2}-SARS2-S(H)-immunized animals. Visualizing significantly enriched GO categories that were unique to Alum+S-treated animals revealed a profile of dysregulated gene classes that likely contributes to the observed vaccine-associated pathology after superinfection (Figure 2C, right panel).

We next visualized fold change in expression of differentially induced genes, considering their associated cellular functions (Figure 2D). These analyses led us to further explore normalized expression of a refined subset of genes that exhibited unique induction profiles and likely contribute to the vaccine-associated immunopathogenesis (Figure 2E). While the suite of genes involved in eosinophil chemotaxis were similarly upregulated under all conditions, uncontrolled induction of the major eosinophil chemotaxin *Ccl11* (eotaxin-1) mRNA was unique to the Alum+S cohort (Figure 2E). Furthermore, T_H2 cytokine mRNAs *Il4*, *Il5*, *Il13*, and *Il19* were potently induced in the majority of Alum+S-vaccinated animals but largely undetectable in the other groups. These analyses pinpoint likely transcriptional mediators underlying VAERD and hyperinflammation after T_H2-biased

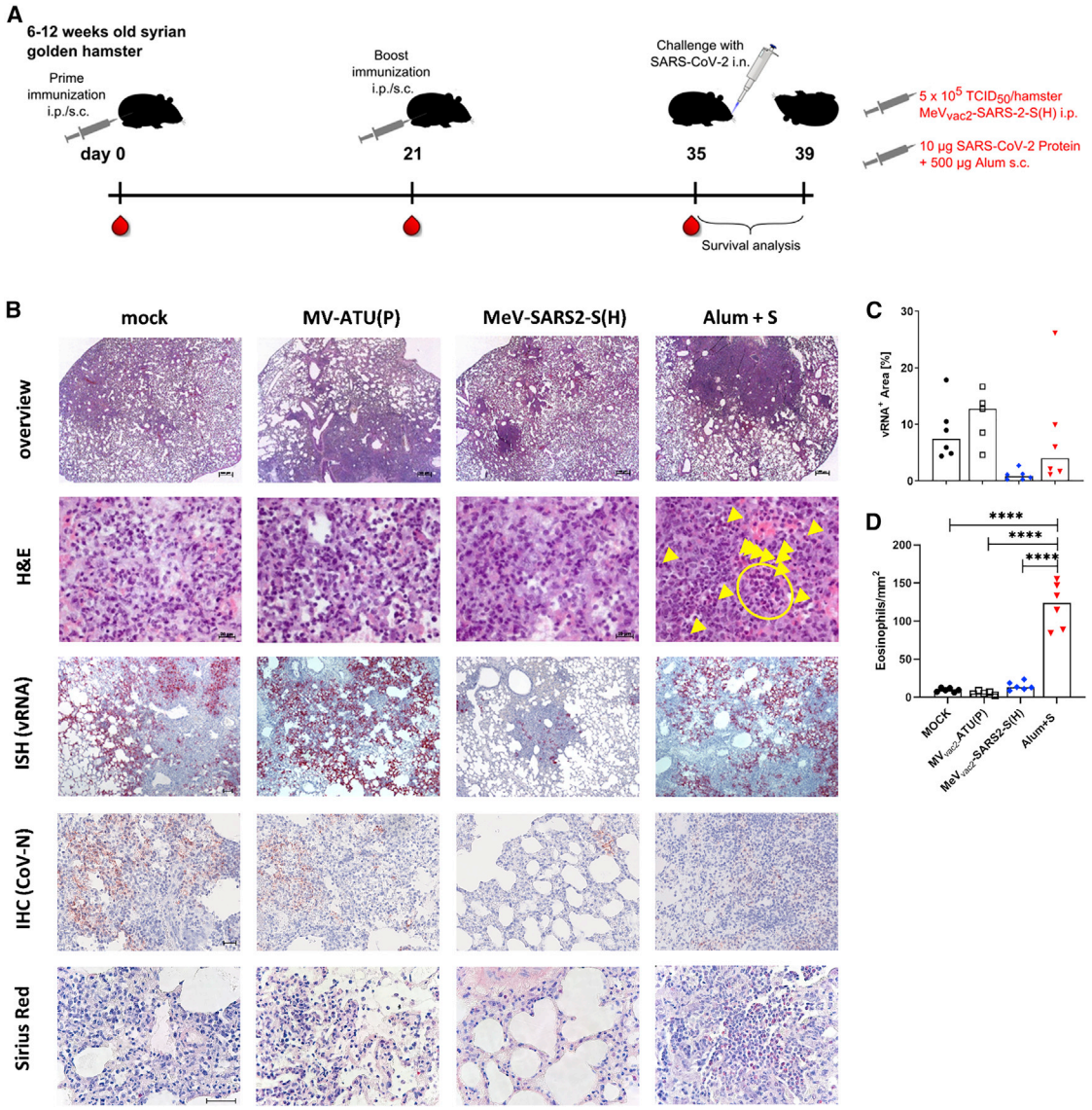

Figure 1. Pulmonary pathology in vaccinated Syrian hamsters upon challenge with SARS-CoV-2

(A) Schematic depiction of experiment. Syrian hamsters were bled and subsequently immunized with indicated vaccines on days 0 and 21 (n = 6/cohort). On day 35, immunized hamsters were bled and intranasally challenged with low-passage SARS-CoV-2 and observed for another 4 days before sacrifice for organ preparation.

(B) Depicted are representative sections of left lobes of vaccinated hamster lungs prepared 4 days post infection (dpi) with low-passage SARS-CoV-2 (n = 6). H&E staining (two top rows) reveals histopathological changes and immune cell infiltration. *In situ* hybridization (ISH) for SARS-CoV-2 viral RNA (third row) and immunohistochemistry (IHC) staining for SARS-CoV-2 nucleocapsid protein N (fourth row) depict extent of infection, while Sirius red staining (bottom row) reveals infiltration of eosinophils (scale bars: top row, 500 µm; second row, 20 µm; other rows, 40 µm). Yellow arrowheads and yellow circle depict individual eosinophils or a cluster of eosinophils in H&E-stained samples, respectively.

(C) Quantification of lung infection by determining the relative area of tissue staining positive by ISH by automated image evaluation of the whole slices.

(D) Eosinophil quantification for all animals is depicted. Eosinophil numbers in 10 randomly selected fields of view at 200× magnification were counted, and means were correlated against the area of view. Each data point reveals the mean number of eosinophils per mm^2 in individual animals. For statistical analysis, ordinary one-way ANOVA was applied with Tukey's multiple comparisons test. ****$p < 0.0001$.

(C and D) Single dots represent individual animals, bars median of groups; black circles, MOCK immunized animals; open squares, MeV vector-immunized animals; blue diamonds, MeV_{vac2}-SARS2-S(H)-immunized animals; red triangles, animals vaccinated with Alum+S. ****$p < 0.0001$.

vaccination: the specific induction of the *Il4/Il5/Il13/Il19* cytokine axis combined with the potent esosinophil chemotaxin *Ccl11* potentially results in uncontrolled recruitment of eosinophils to the site of infection and enhanced pathogenesis.

Induction of T_H2-biased anti-S immunity by alum-adjuvanted protein

To further demonstrate induction of T_H2-biased immunity by vaccination as the trigger of VAERD, hamsters were just

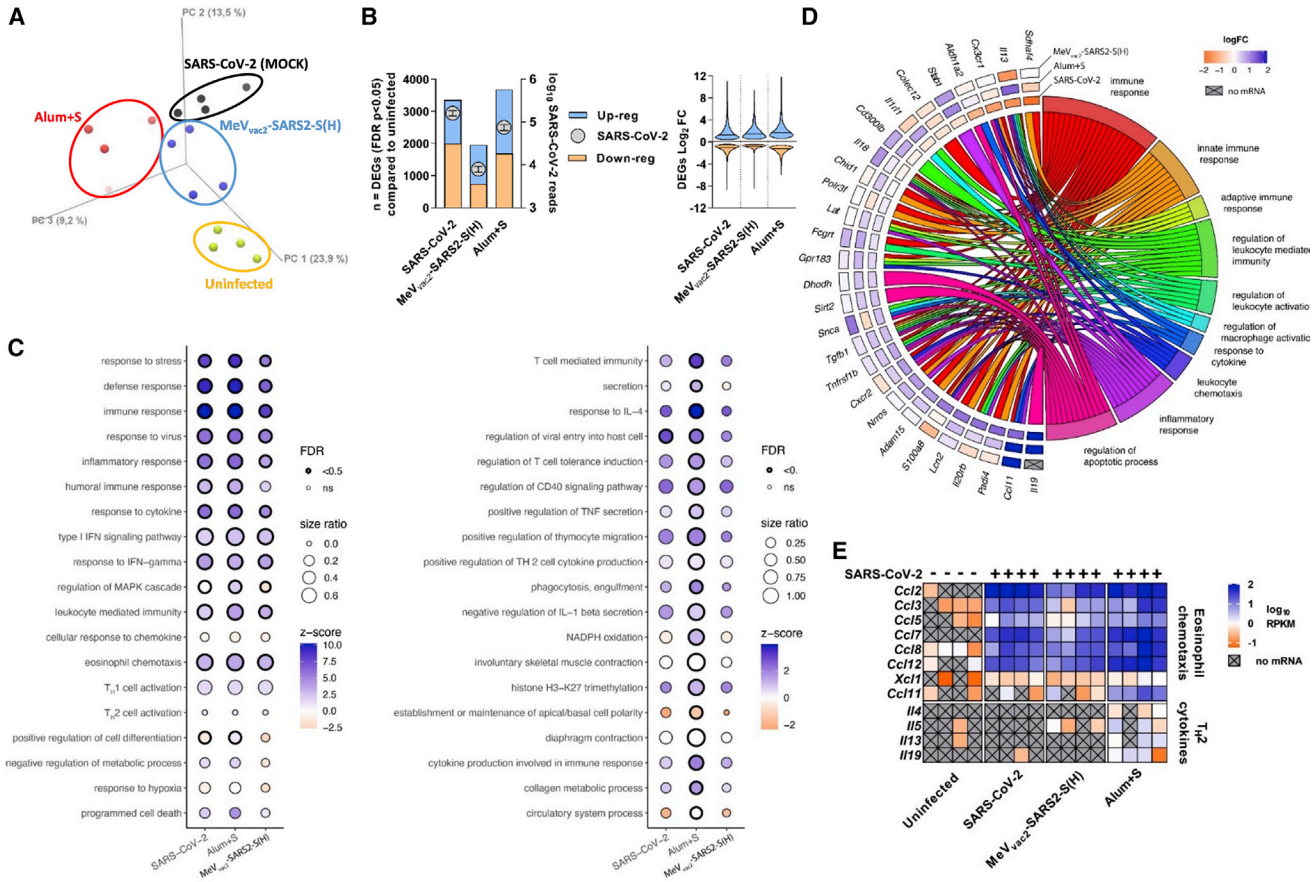

Figure 2. Global host gene dysregulation revealed by global RNA-seq in lungs of infected, differently vaccinated hamsters

(A) Principal component analysis (PCA) of hamster lung transcriptomes. Transcriptomes from individual animals (n = 4/cohort) are represented by a single data point. Yellow, unvaccinated and not infected; blue, unvaccinated and infected; red, vaccinated with MeV$_{vac2}$-SARS2-S(H) and infected; green, vaccinated with alum-adjuvanted protein and infected.

(B) Viral RNA copies and host gene dysregulation in hamster lungs after infection and vaccination. Left panel: data plotted on the left y axis represent the number of differentially expressed genes (DEGs) (false discovery rate [FDR] $p < 0.05$) in the hamster lung under each condition, when compared with uninfected unvaccinated controls (n = 4). Blue: upregulated; orange: downregulated. Data plotted on the right y axis (gray circles) represents the number of lung-resident SARS-CoV-2 mapped reads per condition (mean ± SEM). Right panel: violin plots depict range of $\log_2$ fold change in expression for all significantly dysregulated genes under each condition, when compared with uninfected unvaccinated controls. Horizontal lines, median values.

(C) Gene Ontology (GO) enrichment analysis of SARS-CoV-2-induced DEGs. GO categories are labeled on the y axes. Circle size represents the ratio of significantly dysregulated genes relative to the total gene number in a specific GO term. Circles are shaded relative to activation *Z* score, with significantly enriched categories highlighted. Left panel: selected GO categories related to immune response. Right panel: significant GO categories exclusive to Alum+S-vaccinated animals.

(D) Plot depicting $\log_2$ fold change of 28 identified genes (left) exhibiting differential expression patterns between the different conditions, and their associated cellular function (right).

(E) Dysregulation of selected cytokine genes including eosinophil chemo-attractant *Ccl11* and T$_H$2 cytokine mRNAs in lungs of differently vaccinated hamsters upon SARS-CoV-2 infection. Heatmap represents normalized mRNA expression (reads per kilobase per million bases mapped [RPKM]) of genes. Gray cells with an X represents no detectable mRNA expression (RPKM = 0).

immunized with Alum+S, MeV$_{vac2}$-SARS2-S(H), or medium (MOCK) without SARS-CoV-2 challenge (Figure 3A). We then analyzed antigen-specific cytokine responses of these animals splenocytes' in re-call experiments 14 days after the second immunization.

As a control for successful vaccination, interferon gamma (IFN-γ) secretion was determined. Splenocytes of all animals reacted with IFN-γ secretion after stimulation with the unspecific stimuli Concanavalin A (ConA) or flagellin, which triggered more than 600 spots/10^6 cells in ELISpot, thus demonstrating general functionality. On the other hand, medium- or ovalbumin-stimulated splenocytes showed a background reactivity of 100–250 IFN-γ^+ spots/10^6 cells (Figure 3B). Upon antigen-specific stimulation with recombinant S protein, only animals vaccinated with MeV$_{vac2}$-SARS2-S(H) or alum-adjuvanted S revealed specific reactivity with approximately 400 spots/10^6 cells or in the range of the upper limit of detection, respectively, thereby demonstrating successful induction of cellular immune responses against the SARS-CoV-2 S protein.

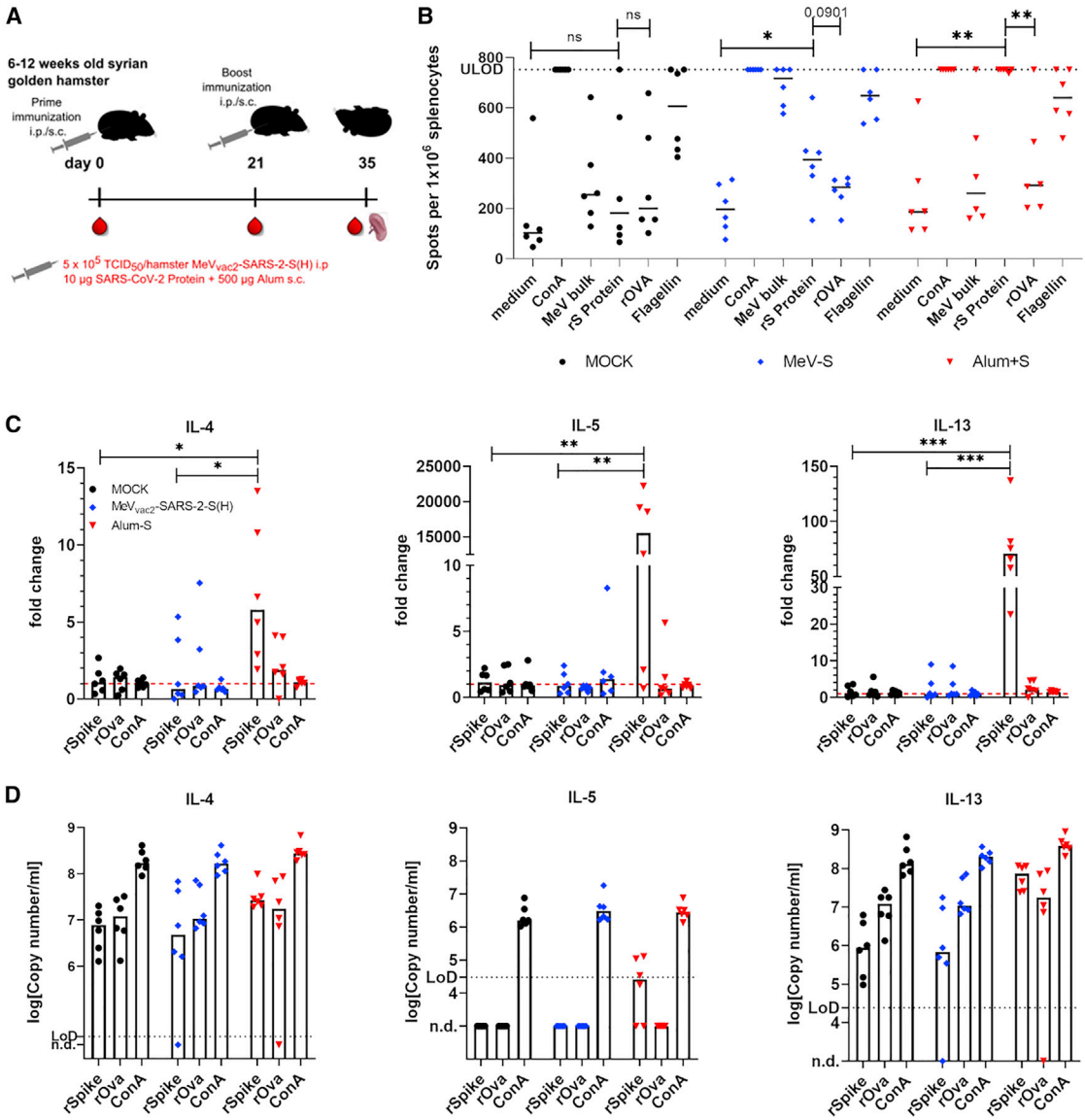

Figure 3. Induction of T_H2-biased antigen-specific immune cells in protein-vaccinated Syrian hamsters

(A) Syrian hamsters were immunized with MeV_{vac2}-SARS2-S(H) (intraperitoneally [i.p.]) or Alum+S (subcutaneously [s.c.]) on days 0 and 21 (n = 6 animals/cohort). Two weeks after immunization, hamsters were sacrificed, blood was collected, and splenocytes were isolated.

(B) IFN-γ ELISpot analysis using splenocytes of hamsters vaccinated on days 0 and 21, isolated 14 days after the boost immunization and after stimulation with recombinant S protein (rS protein) or MeV bulk antigens (MeV bulk). The reactivity of splenocytes was confirmed by Concanavalin A (ConA) (5 µg/mL) or flagellin treatment (20 µg/mL). Recombinant ovalbumin (rOva) or medium served as negative controls. The number of cells per 1×10^6 splenocytes represent the number of cells expressing IFN-γ upon re-stimulation. Dots represents individual animals, horizontals bars median per group (n = 6). Samples above the upper limit of detection (ULOD) were displayed as such. For statistical analysis of grouped ELISpot data, paired t test was applied. ns, not significant ($p > 0.05$); *$p < 0.05$; **$p < 0.01$.

(C) Relative fold change expression of mRNAs encoding IL-4, IL-5, or IL-13 was determined using quantitative RT-PCR and the ΔΔct method. mRNA encoding RPL18 was used as housekeeping gene for normalization. Mean of samples from mock-treated hamsters served as reference. For statistical analysis, ordinary one-way ANOVA was applied with Tukey's multiple comparisons test. ns, not significant ($p > 0.05$), *$p < 0.05$; **$p < 0$ .01; ***$p < 0.001$.

(D) Absolute mRNA copy numbers were determined by quantitative RT-PCR using a plasmid DNA standard for each gene. Mock-vaccinated hamsters, black circles; MeV_{vac2}-SARS2-S(H)-vaccinated hamsters, blue diamonds; protein-vaccinated hamsters, red triangles.

In the absence of suitable assays to quantify hamster IL-4, IL-5, or IL-13 protein, we determined mRNA copy numbers of these cytokines by quantitative RT-PCR in re-stimulated splenocytes and correlated the signals to the hamster housekeeping gene *RPL18* mRNA copies. The total RNA from re-stimulated splenocytes was subjected to analysis (Figure 3C). For normalization, data are presented relative to the average signal in mock-immunized hamsters' splenocytes after the respective stimulation (Figure 3D). S-specific induction of *Il4* (5-fold), *Il5* (>15,000-fold), or *Il13* (70-fold) mRNA was only detected in

splenocytes of animals immunized by alum-adjuvanted S and was significantly higher than in splenocytes of MeV-vaccinated animals or naive animals that did not show relevant up-regulation of these T_H2-cytokine genes after re-stimulation.

These data demonstrate that, in contrast to the MeV-derived vaccine, the alum-adjuvanted S protein induced S-specific T_H2-biased immune cells after vaccination, corroborating the hypothesis of VAERD induction after SARS-CoV-2 challenge specifically by Alum+S.

VAERD in hamsters responds to dexamethasone treatment

To further dissect the role of individual lung cell populations during VAERD by scRNA-seq analysis and to evaluate treatment options for VAERD, the initial challenge experiment of vaccinated hamsters was replicated (Figure 4A). Cohorts of 4–6 hamsters were vaccinated as before with alum-adjuvanted S, MeV_{vac2}-SARS2-S(H), or medium (MOCK). For the cohort receiving Alum+S, the number of animals was doubled to assess the impact of treatment with the clinically used immunosuppressant dexamethasone.

To control immunization and to stratify the cohorts, sera of immunized animals were tested for binding Abs by ELISA and neutralizing Abs by titration of VNT (Figure S3). As expected, immunity against MeV was detected solely after vaccination with MeV_{vac2}-SARS2-S(H). Binding Abs to SARS-CoV-2 S were detected in sera from all animals that received either adjuvanted protein or the MeV-derived vaccine (Figure S3B). However, neutralizing activity inhibiting SARS-CoV-2 was evident only in hamsters immunized with recombinant MeV_{vac2}-SARS2-S(H) (VNT of 10–80), but not in the protein-vaccinated animals (Figure S3H). The binding Ab titers targeting SARS-CoV-2 S were used together with the animals' sex to stratify both Alum+S cohorts for treatment with dexamethasone upon challenge or not. All animals were challenged 14 days after the second vaccination. During the next 4 days, one of both groups that had received Alum+S were treated twice daily with dexamethasone.

Upon infection, weight loss was initially observed in all groups (Figures 4B and S4A). Consistent with previous observations, hamsters immunized with MeV_{vac2}-SARS2-S(H) stopped losing weight by day 2 post infection (p.i.) and recovered thereafter, while naive animals revealed progressive weight loss. This was also evident for hamsters immunized with the protein vaccine that showed comparable decay. Remarkably, the protein-vaccinated, infected animals treated with dexamethasone revealed another phenotype: weight loss stopped on day 2.5, and the animals' weights stabilized over the next 2 days. All animals were sacrificed on day 4 p.i. for subsequent necropsy.

Analysis of gross pathology replicated the phenotype observed previously (Table S2), with signs of pneumonia and inflamed areas on the lungs of naive animals, while MeV_{vac2}-SARS2-S(H)-immunized hamsters showed few lesions on the lungs' surface (Figure S4B). Moreover, this experiment replicated VAERD as evident already by the overall pathology, with large areas of inflammation on the surface of the S-protein-vaccinated animals' lungs and a swollen appearance of the entire lung. This effect was prevented in the dexamethasone-treated animals. Their lungs were comparable to the lung explants of the MeV_{vac2}-SARS2-S(H)-immunized cohort. Lungs were subjected to bronchoalveolar lavage (BAL) and subsequently sampled.

Histopathologic analyses of lung samples after H&E, ISH, immunohistochemistry, and Sirius red staining exactly replicated the VAERD phenotype for Alum+S-vaccinated animals and the absence thereof in MeV_{vac2}-SARS2-S(H)-vaccinated animals (Figure 4C). When Alum+S-immunized animals were treated with dexamethasone, the VAERD phenotype was lost. In these samples, the inflammatory phenotype was absent and lung tissue reflected the appearance of MeV_{vac2}-SARS2-S(H)-immunized hamsters, while the pathology score decreased significantly (Figure 4D). Despite this normalization of lung pathology, immunohistochemistry for SARS-CoV-2 N or ISH for SARS-CoV-2 genomes was not markedly different from naive challenged animals and was enhanced when compared with Alum+S-vaccinated, challenged hamsters without dexamethasone treatment (Figure 4C, last column).

Furthermore, live-virus titers and viral RNA copy numbers, as determined in lung tissue (Figures 5A and 5B) and BAL cells (Figure 5C), were in agreement with this phenotype. Virus RNA copy numbers in lung tissue were significantly reduced in hamsters vaccinated with MeV_{vac2}-SARS2-CoV (0.36–8.28 E-gene copies/RPL18 copy) compared with naive infected animals (110.8–235.3 E-gene copies/RPL18 copy), consistent with the absence of live virus in the lungs of all animals in the MeV group (Figure 5A). Compared with naive/unvaccinated infected hamsters, viral burden was lower in hamsters immunized with Alum+S but increased slightly when these hamsters were treated with dexamethasone during the challenge. Comparable virus RNA copy numbers were obtained for the BAL cells studied.

Thus, viral loads and extent of tissue infection did not correlate with the inflammatory phenotype of pathology, consistent with an immunopathogenesis as the basis for VAERD, which again was not observed for the T_H1-biased MeV-COVID-19 model vaccine candidate. Moreover, the responsiveness of the pathology to dexamethasone treatment indicates a role for immune cells in this process.

Dysregulation of T_H2 cytokines in lungs and BAL cells

To confirm pulmonary up-regulation of *Il4*, *Il5*, *Il13*, and *eotaxin-1* mRNAs in protein-vaccinated animals and to determine if this dysregulation was also observed in BAL cells after infection, total RNA from the respective cells was subjected to quantitative RT-PCR (qRT-PCR). These analyses revealed significant induction of all four cytokine genes in lung cells and revealed the same tendency in BAL cells after infection of protein-vaccinated animals. In contrast, vaccination with the T_H1-biased MeV_{vac2}-SARS2-S(H) down-regulated expression of these critical genes, while dexamethasone treatment did not alter the cytokine expression pattern (Figure S5). Therefore, induction of T_H2 cytokines in protein-vaccinated animals identified by RNA-seq in the first experiment was confirmed in this second cohort of hamsters.

Assignment of dysregulation to individual cells in lungs by scRNA-seq

To delineate the role of individual cell populations, scRNA-Seq data of infected lungs were generated and first analyzed to determine cellular subsets according to individual cellular gene

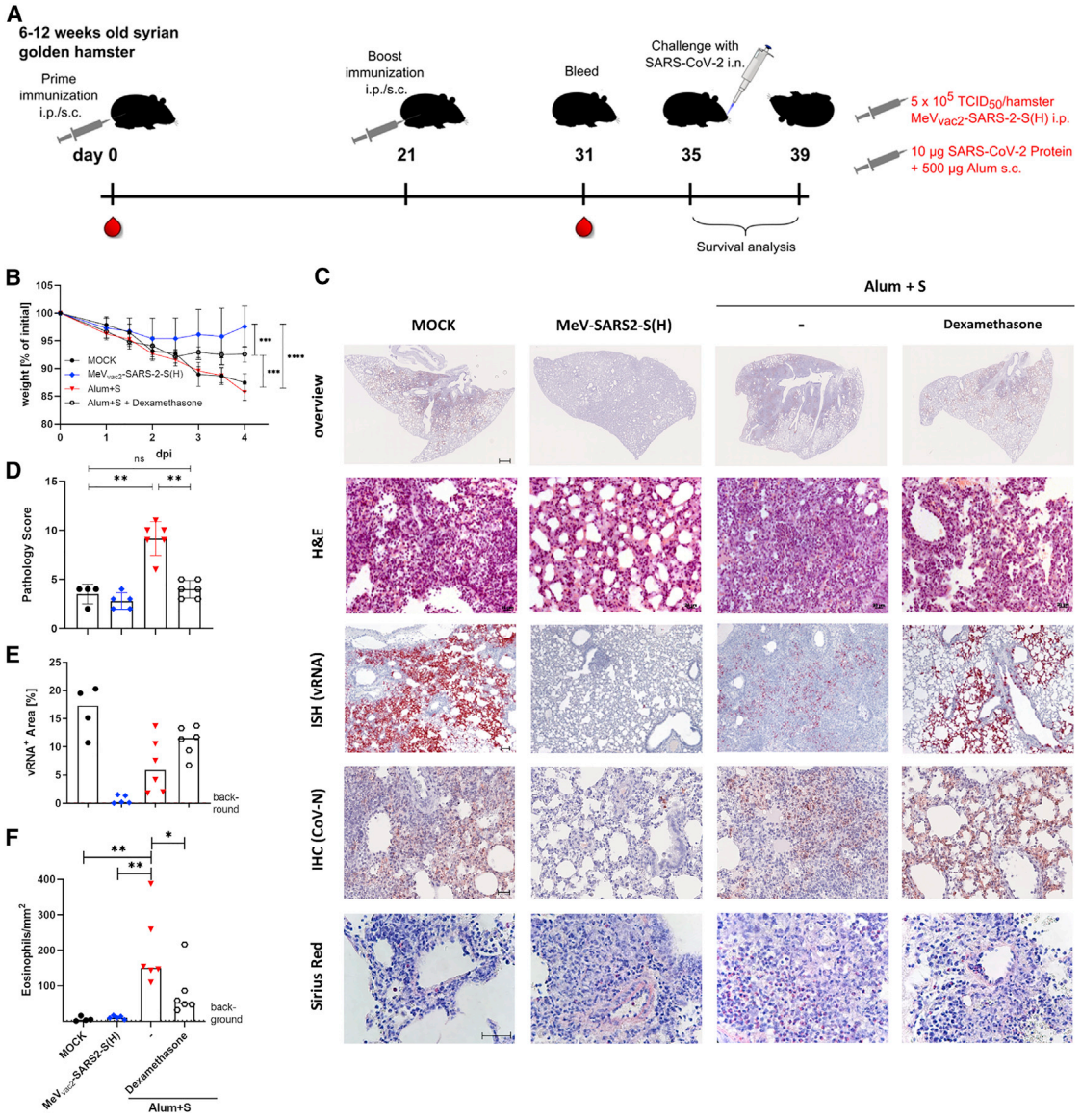

Figure 4. Protection of vaccinated hamsters and pathology upon SARS-CoV-2 challenge in combination with dexamethasone treatment

(A) Schematic depiction of experimental setting. Syrian hamsters were bled and subsequently immunized with indicated vaccines on days 0 and 21 (n = 4 for mock, n = 5 for MeV_{vac2}-SARS2-S(H), n = 6 for both Alum+S-vaccinated cohorts). Ten days after the second immunization, hamsters were bled again. On day 35, immunized hamsters were intranasally challenged with low-passage SARS-CoV-2 and observed for another 4 days before sacrifice for organ preparation.

(B and C) Protective efficacy of vaccination was analyzed by (B) quantifying weight loss over time and (C) histopathology of lung sections prepared 4 dpi (scale bars: top row, 1 mm; second row, 20 µm; all other rows, 40 µm). For statistical analysis, two-way ANOVA was applied with Tukey's multiple comparisons test. ***$p < 0.001$; ****$p < 0.0001$.

(D) Blinded histopathological analysis of H&E-stained lung samples (C, second row) was performed, and findings were scored. For statistical analysis, ordinary one-way ANOVA was applied with Mann-Whitney test. ns, not significant; **$p < 0.01$.

(E) Infected areas positive by ISH against SARS-CoV-2 viral RNA (C, third row) were quantified by determining the relative area of tissue staining positive for viral RNA by automated image evaluation of whole slice. Infection was confirmed by IHC against SARS-CoV-2 nucleocapsid protein (C, fourth row).

(F) Infiltration of eosinophils positive by Sirius red staining (C, bottom row) was quantified by determination of the mean number of eosinophils per mm^2 for each animal. Eosinophils of 10 randomly selected fields of view at 200× magnification were counted, and mean was correlated against the area of view. For statistical analysis, ordinary one-way ANOVA was applied with Tukey's multiple comparisons test. *$p < 0.05$; **$p < 0.01$. Mock-immunized, black circles; MeV_{vac2}-SARS2-S(H), blue diamonds; Alum+S without (red triangles) or with (open circles) dexamethasone treatment.

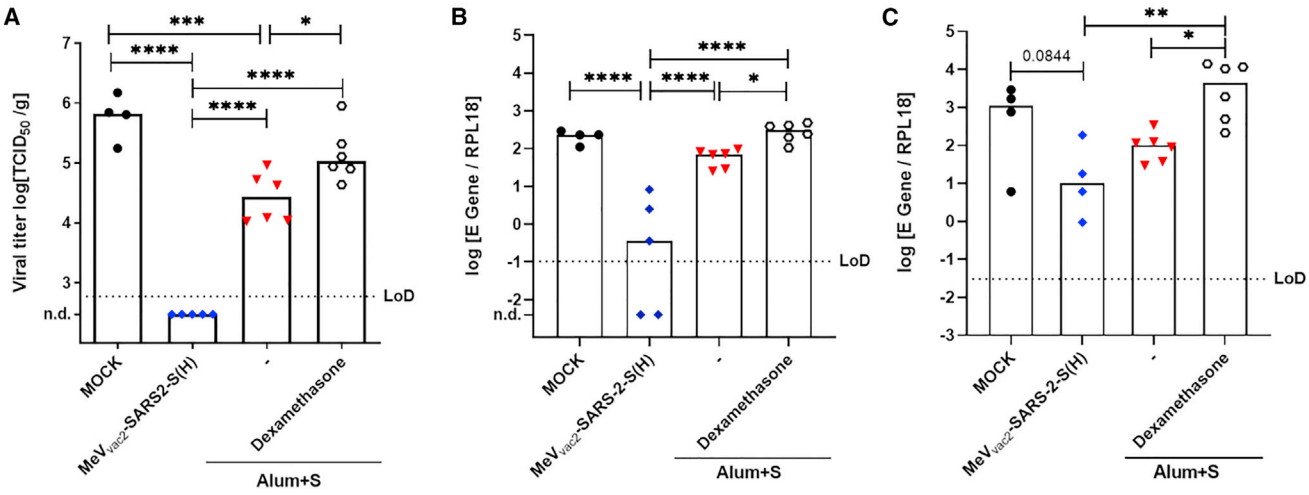

Figure 5. Impact of vaccination or dexamethasone treatment on SARS-CoV-2 titers upon challenge of Syrian hamsters

Protection of vaccinated hamsters upon challenge with SARS-CoV-2 was analyzed 4 dpi by (A) titration of live-virus titers in lung tissue or (B and C) determination of relative SARS-CoV-2 E gene copy numbers in (B) lung tissue or (C) bronchoalveolar lavage (BAL) cells by quantitative RT-PCR. *RPL18* housekeeping gene copies were used for normalization. Lower LoDs are indicated by dotted lines. Each data point represents an individual animal vaccinated with medium (black circles), MeV_{vac2}-SARS2-S(H) (blue diamonds), or alum-adjuvanted S protein without (red triangles) or with (open circles) dexamethasone treatment. For statistical analysis, ordinary one-way ANOVA was applied with Tukey's multiple comparisons test. ns, not significant ($p > 0.05$); *$p < 0.05$; **$p < 0.01$; ***$p < 0.001$; ****$p < 0.0001$.

expression profiles, as described previously (Nouailles et al., 2021). Accordingly, 25 individual cell clusters were defined, and their transcriptional profiles identified 13 different cell populations including immune cells (Figure 6B). Minor differences between vaccine cohorts became evident in the relative cell frequencies in the infected lungs. In naive animals, and even more so in Alum+S-vaccinated animals, lung macrophages, which revealed traits of an interstitial macrophage phenotype, were overrepresented compared with the MeV-vaccinated group. In contrast, alveolar macrophages were observed at higher frequencies in MeV-vaccinated animals' lungs (Figure 6C).

The gene-expression profiles of these distinct cell populations showed specific patterns (Figure 6D). Exclusive up-regulation of *Ccl11* expression in the Alum+S group could be assigned to the overrepresented lung macrophages (Figure 6D). Induction of *Il4*, *Il5*, and *Il13* became evident exclusively in the population of T and natural killer (NK) cells (Figure 6D, three top panels). Zooming in on specific T/NK cell subsets (Figures 6E and 6F), up-regulation of *Il4* was found in regulatory T cells, while *Il5* and *Il13* expression was assigned to cells with an innate lymphoid cell phenotype (Figure 6G) and activated T cells (Table S3). In contrast, MeV_{vac2}-SARS2-S(H)-vaccinated animals reflected a similar, but dampened, response when compared with naive infected animals, with few genes being differentially regulated. On the other hand, monitoring the distribution of SARS-CoV-2 RNA sequences indicating virus infection or uptake revealed a broad distribution of viral RNA in most cell types in naive/unvaccinated, infected animals (Figures 7A and 7B). This distribution was more focused in lung macrophages in Alum+S-vaccinated animals and correlated to some extent with the expression profiles of Fcγ receptors IIb and IV, which were found to be specifically up-regulated after infection in both naive and Alum+S-vaccinated samples (Figure 7C).

To further mine the scRNA-seq data, we performed both gene set variation analysis (GSVA) and gene set enrichment analysis (GSEA) using the REACTOME, KEGG, and GO databases on specific cell populations that contribute to the VAERD observed in Alum+S-vaccinated animals (Figures S6 and S7), focusing on alveolar macrophages, lung macrophages, monocytic macrophages, *Treml4*$^{+}$ monocytes, and T/NK cells. For GSVA, normalized, by-cell-population gene-expression values were used as input, while DEGs between the unvaccinated and either Alum+S- or MeV_{vac2}-SARS2-S(H)-vaccinated conditions were utilized for GSEA. These analyses highlight pathways and biological processes, which are induced by SARS-CoV-2 infection and are differentially targeted or regulated across these selected cell types, dependent on prior immune status and vaccination type. These supportive analyses of the hamster lung scRNA-seq data provide insights into how the observed transcriptional differences mediate their downstream effects, exhibiting differential targeting of a broad range of cellular process or canonical pathways in a cell-type-specific manner.

Taken together, the scRNA-seq data assigned the up-regulation of IL-4, IL-5, and IL-13 to specific T cell subpopulations induced by vaccination with Alum+S, while CCL-11 and IL-19 expression was contributed by lung macrophages, which were overrepresented, revealed up-regulation of Fcγ receptors, and were the main target population containing an excess of SARS-CoV-2 RNA. These aberrant patterns of dysregulated gene expression were not observed in animals vaccinated with the prototypic T_H1-biased MeV-COVID-19 vaccine candidate.

DISCUSSION

Based on these data, we propose the following immune-cell-mediated mechanism for induction of VAERD: vaccination with

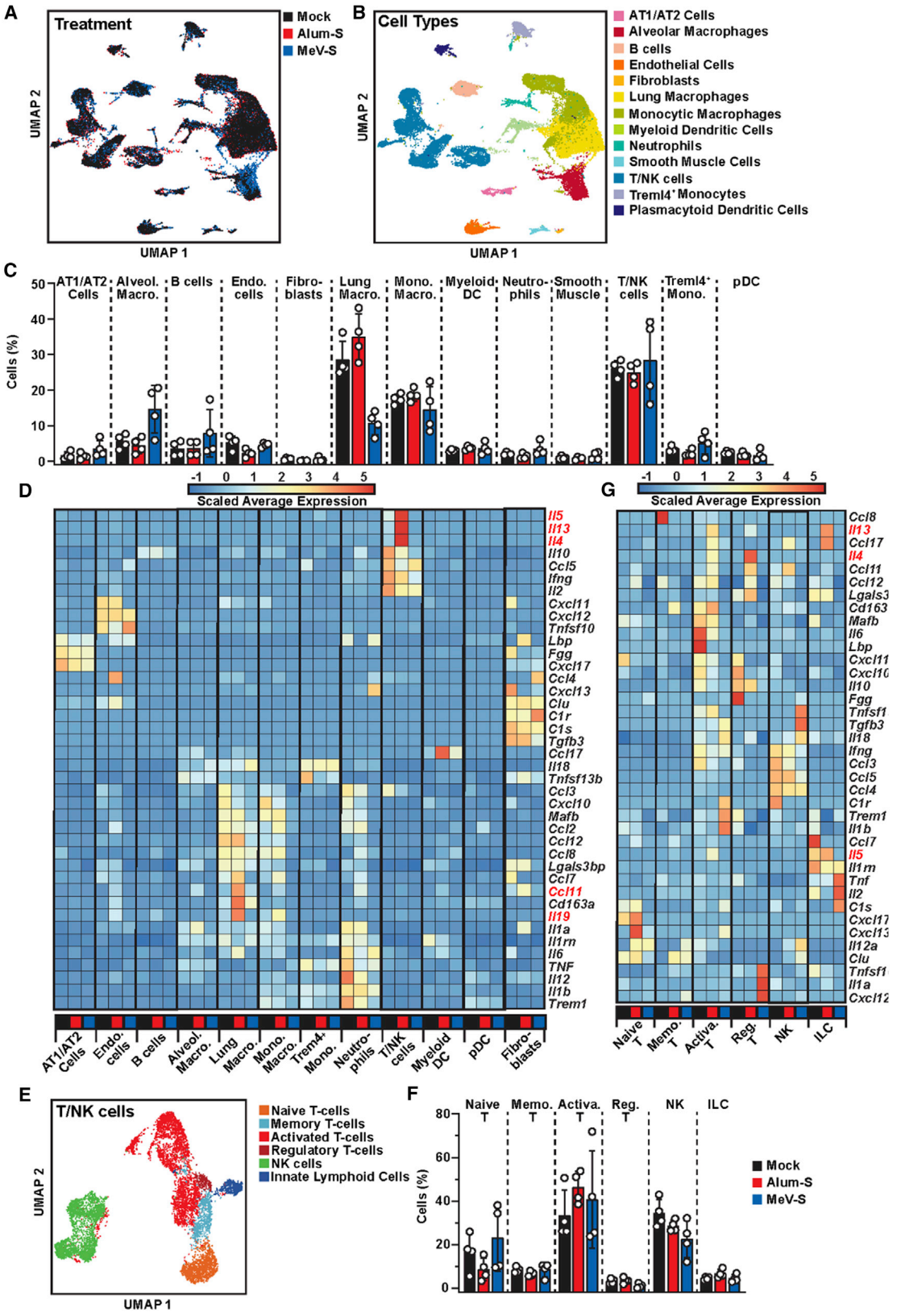

(legend on next page)

alum-adjuvanted S protein in de-folded conformation induces low levels of non-protective S-specific binding Abs lacking neutralizing activity. In parallel, T_H2-biased S-specific T cell responses were induced as evidenced by the significant up-regulation of IL-4, IL-5, and IL-13 after recall. After infection, these immune responses lowered the virus load to some extent, but the induction of T_H2 immunity promoted VAERD via the IL-4/IL-5/IL-13 chemokine axis secreted by regulatory T cells and innate lymphoid cells. These processes are likely reinforced by IL-19 secreted by hyperstimulated lung macrophages, which, in addition, express further chemo-attractants such as CCL-11, the major attractant of eosinophils. Indeed, massive infiltration of eosinophils completed the picture of VAERD. Macrophage activity correlated with SARS-CoV-2 virus genome enrichment. It is therefore tempting to hypothesize that the enrichment of SARS-CoV-2 RNAs in macrophages is caused by Fcγ-receptor-mediated uptake of opsonized viruses as previously proposed for ADE processes and recently demonstrated for enrichment of SARS-CoV-2 in monocytes of the peripheral blood of patients with severe COVID-19 (Junqueira et al., 2022).

While our data support such a model for induction of VAERD by sub-optimal T_H2-biased prototypic vaccines targeting SARS-CoV-2, the nature of these findings seems quite striking. VAERD had been clearly observed for both MERS-CoV and SARS-CoV in the respective transgenic mouse models after vaccination with T_H2-biased, whole-inactivated virus vaccines (Bolles et al., 2011; Tseng et al., 2012; Iwata-Yoshikawa et al., 2014; Honda-Okubo et al., 2015; Agrawal et al., 2016). Since no human vaccines had been tested against these two pathogens, the transferability of these findings to the occurrence of VAERD in humans remained unclear. Nevertheless, this potential risk was perceived also for vaccine-induced immune responses that target the closely related SARS-CoV-2 and triggered vaccine developers to aim for T_H1-biased immunity and to assess the potential of immunopathogenesis in the available animal models (Anderson et al., 2020; Corbett et al., 2020a, 2020b; Jackson et al., 2020; Polack et al., 2020; Ramasamy et al., 2020; Walsh et al., 2020; Sadoff et al., 2021; Stephenson et al., 2021; van der Lubbe et al., 2021). Despite all these efforts, only two studies have been published so far that revealed evidence for VAERD potential upon vaccination of T_H2-prone BALB/c mice with denatured antigen followed by a challenge with a mouse-adapted recombinant SARS-CoV-2 (DiPiazza et al., 2021; Iwata-Yoshikawa et al., 2022). While using an unbiased animal model and non-adapted SARS-CoV-2 and going beyond the mechanistic hypotheses expressed (Iwata-Yoshikawa et al., 2022), our study aligns well with these mouse data in the observed VAERD phenotype with T_H2 cytokine secretion and massive eosinophil attraction. However, no other studies so far have identified evidence for the risk of enhanced disease upon COVID-19 vaccination. How can this discrepancy be explained?

The sub-optimal immunization regime of vaccinating Syrian hamster subcutaneously with alum-adjuvanted, non-stabilized S protein was expected to give a rather mediocre (Nürnberger et al., 2019), but T_H2-biased, immune response (Ko et al., 2017) as a worst-case control in our earlier study describing a MeV-derived COVID-19 vaccine candidate (Hörner et al., 2020). Indeed, only binding Abs with no neutralizing activity were induced, and no antigen-specific $CD8^+$ T cell killing activity was observed by us (Hörner et al., 2020) or others (DiPiazza et al., 2021; Iwata-Yoshikawa et al., 2022). Our observations thereby closely resemble VAERD induced by inactivated RSV (Johnson and Graham, 1999; De Swart et al., 2002; Johnson et al., 2003, 2004; Moghaddam et al., 2006) or MeV in the respective animal models (Polack et al., 2003), which are quite reminiscent of the situation observed in human VAERD after RSV (Openshaw, 2001) or measles vaccination (Nader and Warren, 1968) using whole-inactivated virus vaccines. Moreover, induction of protective immune responses, or in the worst-case scenario, immunopathogenesis, represents a complex interplay of innate immune processes that set the stage for humoral and cellular adaptive immunity. This can also be deduced from our data. While dexamethasone did not inhibit T_H2 cytokine expression, here, it clearly reduced pathology in the VAERD setting, in addition to naive infected hamsters (Wyler et al., 2022; Yuan et al., 2022). Thereby, a quite delicate process is revealed, balancing immune activities destructive against pathogen or host tissue, which may be difficult to trigger.

Limitations of the study

As already pointed out by DiPiazza et al., drawing conclusions from animal models and extending these observations to the immunological situation in humans may be a difficult task (DiPiazza et al., 2021). However, we were able to replicate VAERD induced by a protein-based COVID-19 vaccine candidate with a very similar phenotype in a second animal model, Syrian hamsters, using an unmodified low-passage virus isolate. Therefore, our data strongly support the idea of monitoring vaccinated human patients that experience a break-through infection closely. In any case, while our experimental vaccines mimic, but are not the same as, the authorized vaccines, these and previously published data point to few concerns for vaccines developed to trigger T_H1-biased responses such as viral vector platform-based vaccines, mRNA vaccines, or other vaccine concepts developed for such bias by, e.g., using respective adjuvants. Moreover, even if VAERD as observed in our model should occur in human patients, this immunopathology would be treatable by dexamethasone, which was confirmed to be an effective medication for severe courses of COVID-19 anyway (Tomazini

Figure 6. Annotation of cell populations in infected hamster lungs and respective gene regulation

(A–C) Definition (A), annotation (B), and proportion (C) of specific cell populations found in the lungs of differently vaccinated hamsters 4 dpi with SARS-CoV-2 (n = 4).

(D) Differentially regulated genes of interest in these cell populations are displayed in the presented heatmap.

(E–G) To further pinpoint dysregulation of T or NK cells, the respective cell subsets were (E) annotated according to maker genes, (F) quantified, and (G) dysregulation of genes was resolved in the respective heatmap as displayed.

(A, C, D, F, and G) Black, mock-vaccinated hamsters; red, hamsters vaccinated with Alum+S; blue, hamsters vaccinated with MeV_{vac2}-SARS2-S(H) (MeV-S).

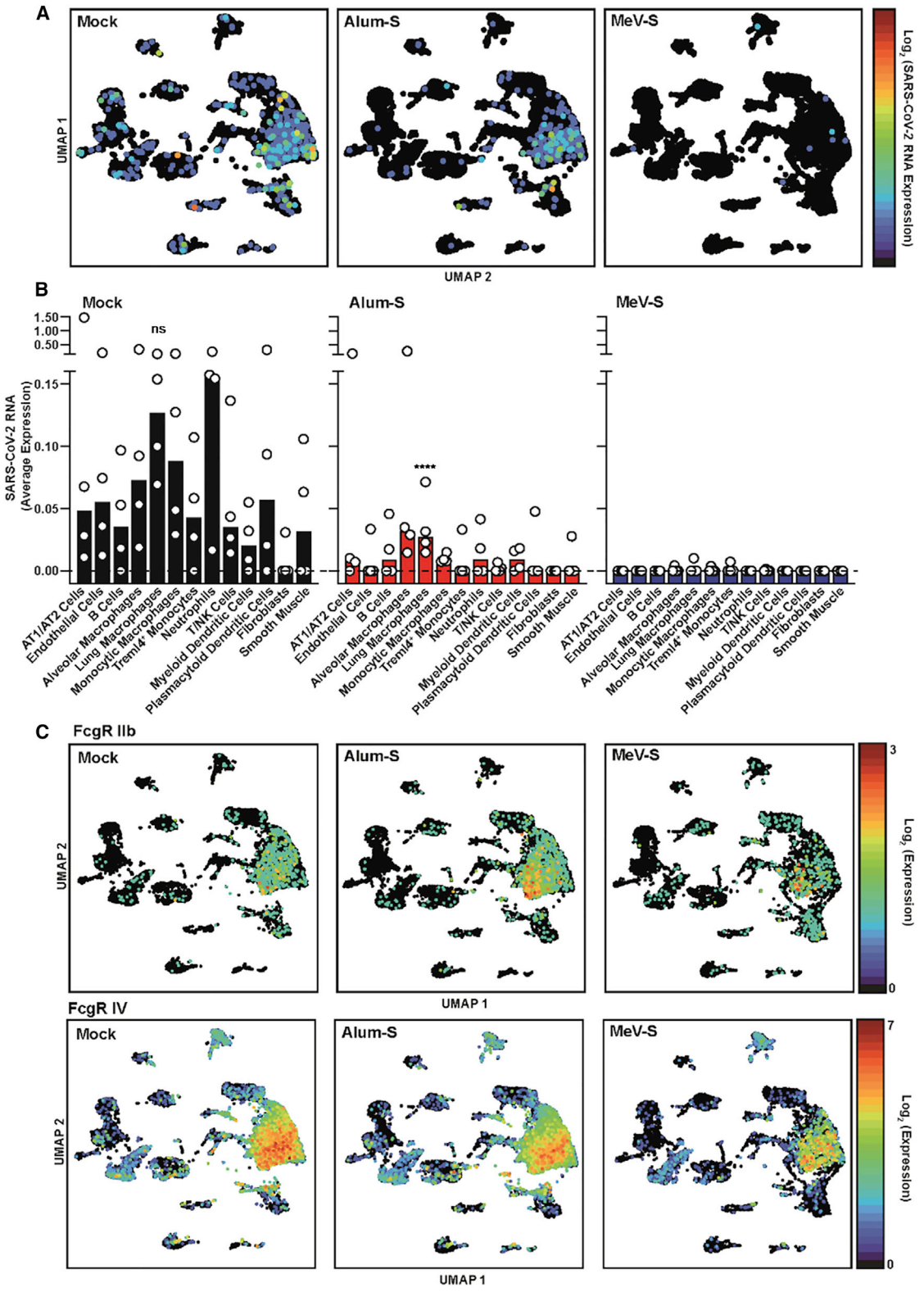

(legend on next page)

et al., 2020; Horby et al., 2021). This would be good news also for putative VAERD being mistakenly diagnosed as a variant of the usual forms of severe COVID-19 in a naive patient.

A further limitation of our study is the restriction of our analyses to a single time point of disease. It would be interesting to analyze further progression of the animals with or without VAERD. However, the applied challenge model is rather harsh. The hamsters lose weight after infection with a highly reproducible kinetics that necessitates sacrifice of 50%–83% of naive animals due to humane endpoints 5 to 6 days after infection (Hörner et al., 2020), and statistically significant differences cannot be expected by realistic animal numbers. Therefore, day 4 after infections was chosen as the day of analyses since this is the time point during infection when most dramatic effects can be expected (measurable weight loss starts at day 2 p.i.), but all animals are still available.

In conclusion, our data support the idea that ADE-like processes, as reported by Wan et al. for MERS-CoV, could be relevant in the mechanism of VAERD. For MERS-CoV, a monoclonal Ab binding to the RBD of the S is able to cross-link MERS-CoV S and Fc receptors. When tested in a pseudovirus assay, this monoclonal Ab mediated virus entry into CD32A-expressing (i.e., FcγRIIA-positive) cells and macrophages (Wan et al., 2020). Such an uptake mechanism would explain the enrichment of SARS-CoV-2 genomes in macrophage populations correlating with the Fc-receptor distribution as observed in our study. Recent clinical data have demonstrated evidence that monocytes in the peripheral blood of patients with severe COVID-19 take up opsonized SARS-CoV-2 particles via this route and are impacted by this process (Junqueira et al., 2022). In any case, enrichment of SARS-CoV-2 in and stimulation of this immune cell population result in the secretion of the major eosinophil attractant CCL-11 and IL-19, which can drive regulatory T cells (T_{reg}s) into T_H2 polarization. Together with the IL-4/IL-5/IL-13 chemokine axis of such S-specific T_H2-biased CD4 helper cell populations, CCL-11 can be expected to cause infiltration of eosinophils in a process mechanistically reminiscent of allergic asthma, resulting in the immunopathogenesis observed in our study.

STAR★METHODS

Detailed methods are provided in the online version of this paper and include the following:

SUPPLEMENTAL INFORMATION

Supplemental information can be found online at https://doi.org/10.1016/j.celrep.2022.111214.

ACKNOWLEDGMENTS

The authors would like to thank Daniela Müller, Mona Lange, and Silvia Schuparis for excellent technical assistance, Bevan Sawatsky for support of BSL-3 procedures, Elke Völker for assistance with circular dichroism (CD) spectroscopy, the team of the animal husbandry for logistic support with hamster experiments, and Christoph Schürmann for scientific discussions. The authors are indebted to Klaus Cichutek for intramural funding and support and to Stefan Schülke for providing recombinant ovalbumin and flagellin A. The SARS-CoV-2 trimeric spike (cat. no. 101007) was obtained from the National Institute for Biological Standards and Control, UK. Our thanks go to Dr. Barney S. Graham, NIAID, and Chris Ball, NIBSC, for providing this protein. This work was supported by grants from the German Center for Infection Research (DZIF; TTU 01.805 and TTU 01.922_00) and the German Ministry of Health (CHARIS) to M.D.M. and by funding of Berlin Institute of Health (BIH) to C.G. J.K. is supported by the Center of Infection Biology and Immunity (ZIBI) and Charité PhD Program. G.N. is supported by the German Federal Ministry of Education and Research and by the Agence Nationale de la Recherche (ANR) in the framework of MAPVAP (16GW0247). D.T. is supported by the (BMBF grant 01KI2106). A.G. is supported by the DFG, grant 398066876-GRK 2485/1.

AUTHOR CONTRIBUTIONS

Conceptualization, C.H., G.N., R.J.P.B., and M.D.M.; acquisition of funding, M.D.M. and R.J.P.B.; data curation, D.T., A.G., D.P., and R.J.P.B.; investigation, A.E., S.M., J.K., A.A., M.A., P.G., M.N., R.P., C.M., M.G.S., A.B., C.K., E.W., A.K., and M.D.M.; analysis of sequencing data, D.T., A.G., D.P., C.M., E.W., and R.J.P.B.; visualization, A.E., J.K., D.T., D.P., E.W., R.J.P.B., and M.D.M.; supervision, Z.I., Z.W., S.P., M.L., G.N., C.G., R.J.P.B., and M.D.M.; writing - original draft, A.E., R.J.B.P., and M.D.M.; writing - review & editing, all authors.

Figure 7. Assignment of SARS-CoV-2 reads and FcR expression to cell populations in infected hamster lungs

(A and B) Assignment of SARS-CoV-2 genome reads to cell populations defined in Figure 6 (A) and quantification of respective positive cells of the different treatment groups as indicated (B). Single dots represent individual animals. Differential expression of SARS-CoV-2 RNA was analyzed using the Loupe Browser 6.0.0. Statistical significance was tested by comparison of individual cell populations with all other cells within the different treatment groups, p values were adjusted using Benjamini-Hochberg correction for multiple testings. ns, not significant; ****$p < 0.0001$.

(C) Assignment of mRNA reads encoding hamster FcγR IIb (top panel) or FcγR IV (bottom panel) to cell populations defined in Figure 6.

DECLARATION OF INTERESTS

The authors declare no competing interests.

INCLUSION AND DIVERSITY

We worked to ensure sex balance in the selection of non-human subjects. The author list of this paper includes contributors from the location where the research was conducted who participated in the data collection, design, analysis, and/or interpretation of the work.

Received: March 20, 2022
Revised: May 17, 2022
Accepted: July 22, 2022
Published: August 3, 2022

REFERENCES

Agrawal, A.S., Tao, X., Algaissi, A., Garron, T., Narayanan, K., Peng, B.-H., Couch, R.B., and Tseng, C.-T.K. (2016). Immunization with inactivated Middle East Respiratory Syndrome coronavirus vaccine leads to lung immunopathology on challenge with live virus. Hum. Vaccin. Immunother. *12*, 2351–2356.

Anderson, E.J., Rouphael, N.G., Widge, A.T., Jackson, L.A., Roberts, P.C., Makhene, M., Chappell, J.D., Denison, M.R., Stevens, L.J., Pruijssers, A.J., et al. (2020). Safety and immunogenicity of SARS-CoV-2 mRNA-1273 vaccine in older adults. N. Engl. J. Med. *383*, 2427–2438.

Beltramello, M., Williams, K.L., Simmons, C.P., Macagno, A., Simonelli, L., Quyen, N.T.H., Sukupolvi-Petty, S., Navarro-Sanchez, E., Young, P.R., de Silva, A.M., et al. (2010). The human immune response to Dengue virus is dominated by highly cross-reactive antibodies endowed with neutralizing and enhancing activity. Cell Host Microbe *8*, 271–283.

Böhmer, M.M., Buchholz, U., Corman, V.M., Hoch, M., Katz, K., Marosevic, D.V., Böhm, S., Woudenberg, T., Ackermann, N., Konrad, R., et al. (2020). Investigation of a COVID-19 outbreak in Germany resulting from a single travel-associated primary case: a case series. Lancet Infect. Dis. *20*, 920–928.

Bolles, M., Deming, D., Long, K., Agnihothram, S., Whitmore, A., Ferris, M., Funkhouser, W., Gralinski, L., Totura, A., Heise, M., and Baric, R.S. (2011). A double-inactivated severe acute respiratory syndrome coronavirus vaccine provides incomplete protection in mice and induces increased eosinophilic proinflammatory pulmonary response upon challenge. J. Virol. *85*, 12201–12215.

Brown, R.J.P., Tegtmeyer, B., Sheldon, J., Khera, T., Anggakusuma, Todt, D., Todt, D., Vieyres, G., Weller, R., Joecks, S., et al. (2020). Liver-expressed Cd302 and Cr1l limit hepatitis C virus cross-species transmission to mice. Sci. Adv. *6*, eabd3233.

Bussmann, B.M., Reiche, S., Jacob, L.H., Braun, J.M., and Jassoy, C. (2006). Antigenic and cellular localisation analysis of the severe acute respiratory syndrome coronavirus nucleocapsid protein using monoclonal antibodies. Virus Res. *122*, 119–126.

Chen, S., Zhou, Y., Chen, Y., and Gu, J. (2018). fastp: an ultra-fast all-in-one FASTQ preprocessor. Bioinformatics *34*, i884–i890.

Corbett, K.S., Edwards, D.K., Leist, S.R., Abiona, O.M., Boyoglu-Barnum, S., Gillespie, R.A., Himansu, S., Schäfer, A., Ziwawo, C.T., DiPiazza, A.T., et al. (2020a). SARS-CoV-2 mRNA vaccine design enabled by prototype pathogen preparedness. Nature *586*, 567–571.

Corbett, K.S., Flynn, B., Foulds, K.E., Francica, J.R., Boyoglu-Barnum, S., Werner, A.P., Flach, B., O'Connell, S., Bock, K.W., Minai, M., et al. (2020b). Evaluation of the mRNA-1273 vaccine against SARS-CoV-2 in nonhuman primates. N. Engl. J. Med. *383*, 1544–1555.

Corman, V.M., Landt, O., Kaiser, M., Molenkamp, R., Meijer, A., Chu, D.K., Bleicker, T., Brünink, S., Schneider, J., Schmidt, M.L., et al. (2020). Detection of 2019 novel coronavirus (2019-nCoV) by real-time RT-PCR. Euro Surveill. *25*, 2000045.

De Swart, R.L., Kuiken, T., Timmerman, H.H., van Amerongen, G., van den Hoogen, B.G., Vos, H.W., Neijens, H.J., Andeweg, A.C., and Osterhaus, A.D.M.E. (2002). Immunization of macaques with formalin-inactivated respiratory syncytial virus (RSV) induces interleukin-13-associated hypersensitivity to subsequent RSV infection. J. Virol. *76*, 11561–11569.

Del Valle, J.R., Devaux, P., Hodge, G., Wegner, N.J., McChesney, M.B., and Cattaneo, R. (2007). A vectored measles virus induces hepatitis B surface antigen antibodies while protecting macaques against measles virus challenge. J. Virol. *81*, 10597–10605.

DiPiazza, A.T., Leist, S.R., Abiona, O.M., Moliva, J.I., Werner, A., Minai, M., Nagata, B.M., Bock, K.W., Phung, E., Schäfer, A., et al. (2021). COVID-19 vaccine mRNA-1273 elicits a protective immune profile in mice that is not associated with vaccine-enhanced disease upon SARS-CoV-2 challenge. Immunity *54*, 1869–1882.e6.

Espitia, C.M., Zhao, W., Saldarriaga, O., Osorio, Y., Harrison, L.M., Cappello, M., Travi, B.L., and Melby, P.C. (2010). Duplex real-time reverse transcriptase PCR to determine cytokine mRNA expression in a hamster model of New World cutaneous leishmaniasis. BMC Immunol. *11*, 31.

Halwe, S., Kupke, A., Vanshylla, K., Liberta, F., Gruell, H., Zehner, M., Rohde, C., Krähling, V., Gellhorn Serra, M., Kreer, C., et al. (2021). Intranasal administration of a monoclonal neutralizing antibody protects mice against SARS-CoV-2 infection. Viruses *13*, 1498.

Hänzelmann, S., Castelo, R., and Guinney, J. (2013). GSVA: gene set variation analysis for microarray and RNA-seq data. BMC Bioinf. *14*, 7.

Hao, Y., Hao, S., Andersen-Nissen, E., Mauck, W.M., Zheng, S., Butler, A., Lee, M.J., Wilk, A.J., Darby, C., Zager, M., et al. (2021). Integrated analysis of multimodal single-cell data. Cell *184*, 3573–3587.e29.

Holland, C.H., Tanevski, J., Perales-Patón, J., Gleixner, J., Kumar, M.P., Mereu, E., Joughin, B.A., Stegle, O., Lauffenburger, D.A., Heyn, H., et al. (2020). Robustness and applicability of transcription factor and pathway analysis tools on single-cell RNA-seq data. Genome Biol. *21*, 36.

Honda-Okubo, Y., Barnard, D., Ong, C.H., Peng, B.-H., Tseng, C.-T.K., and Petrovsky, N. (2015). Severe acute respiratory syndrome-associated coronavirus vaccines formulated with delta inulin adjuvants provide enhanced protection while ameliorating lung eosinophilic immunopathology. J. Virol. *89*, 2995–3007.

Horby, P., Lim, W.S., Emberson, J.R., Mafham, M., Bell, J.L., Linsell, L., Staplin, N., Brightling, C., Ustianowski, A., Elmahi, E., et al. (2021). Dexamethasone in hospitalized patients with Covid-19. N. Engl. J. Med. Overseas. Ed. *384*, 693–704.

Hörner, C., Schürmann, C., Auste, A., Ebenig, A., Muraleedharan, S., Dinnon, K.H., Scholz, T., Herrmann, M., Schnierle, B.S., Baric, R.S., and Mühlebach, M.D. (2020). A highly immunogenic and effective measles virus-based Th1-biased COVID-19 vaccine. Proc. Natl. Acad. Sci. USA *117*, 32657–32666.

Iwata-Yoshikawa, N., Shiwa, N., Sekizuka, T., Sano, K., Ainai, A., Hemmi, T., Kataoka, M., Kuroda, M., Hasegawa, H., Suzuki, T., and Nagata, N. (2022). A lethal mouse model for evaluating vaccine-associated enhanced respiratory disease during SARS-CoV-2 infection. Sci. Adv. *8*, eabh3827.

Iwata-Yoshikawa, N., Uda, A., Suzuki, T., Tsunetsugu-Yokota, Y., Sato, Y., Morikawa, S., Tashiro, M., Sata, T., Hasegawa, H., and Nagata, N. (2014). Effects of Toll-like receptor stimulation on eosinophilic infiltration in lungs of BALB/c mice immunized with UV-inactivated severe acute respiratory syndrome-related coronavirus vaccine. J. Virol. *88*, 8597–8614.

Jackson, L.A., Anderson, E.J., Rouphael, N.G., Roberts, P.C., Makhene, M., Coler, R.N., McCullough, M.P., Chappell, J.D., Denison, M.R., Stevens, L.J., et al. (2020). An mRNA vaccine against SARS-CoV-2 - preliminary report. N. Engl. J. Med. *383*, 1920–1931.

Johnson, T.R., and Graham, B.S. (1999). Secreted respiratory syncytial virus G glycoprotein induces interleukin-5 (IL-5), IL-13, and eosinophilia by an IL-4-independent mechanism. J. Virol. *73*, 8485–8495.

Johnson, T.R., Parker, R.A., Johnson, J.E., and Graham, B.S. (2003). IL-13 is sufficient for respiratory syncytial virus G glycoprotein-induced eosinophilia after respiratory syncytial virus challenge. J. Immunol. *170*, 2037–2045.

Johnson, T.R., Teng, M.N., Collins, P.L., and Graham, B.S. (2004). Respiratory syncytial virus (RSV) G glycoprotein is not necessary for vaccine-enhanced disease induced by immunization with formalin-inactivated RSV. J. Virol. *78*, 6024–6032.

Junqueira, C., Crespo, Â., Ranjbar, S., de Lacerda, L.B., Lewandrowski, M., Ingber, J., Parry, B., Ravid, S., Clark, S., Schrimpf, M.R., et al. (2022). FcγR-mediated SARS-CoV-2 infection of monocytes activates inflammation. Nature *606*, 576–584.

Kärber, G. (1931). Beitrag zur kollektiven Behandlung pharmakologischer Reihenversuche. Archiv f. experiment. Pathol. u. Pharmakol *162*, 480–483.

Kim, H.W., Canchola, J.G., Brandt, C.D., Pyles, G., Chanock, R.M., Jensen, K., and Parrott, R.H. (1969). Respiratory syncytial virus disease in infants despite prior administration of antigenic inactivated vaccine. Am. J. Epidemiol. *89*, 422–434.

Ko, E.-J., Lee, Y.-T., Kim, K.-H., Lee, Y., Jung, Y.-J., Kim, M.-C., Lee, Y.-N., Kang, T., and Kang, S.-M. (2017). Roles of aluminum hydroxide and monophosphoryl lipid A adjuvants in overcoming CD4+ T cell deficiency to induce isotype-switched IgG antibody responses and protection by T-dependent Influenza vaccine. J. Immunol. *198*, 279–291.

Levin, J.Z., Yassour, M., Adiconis, X., Nusbaum, C., Thompson, D.A., Friedman, N., Gnirke, A., and Regev, A. (2010). Comprehensive comparative analysis of strand-specific RNA sequencing methods. Nat. Methods *7*, 709–715.

Llewellyn, B.D. (1970). An improved Sirius red method for amyloid. J. Med. Lab. Technol. *27*, 308–309.

Malczyk, A.H., Kupke, A., Prüfer, S., Scheuplein, V.A., Hutzler, S., Kreuz, D., Beissert, T., Bauer, S., Hubich-Rau, S., Tondera, C., et al. (2015). A highly immunogenic and protective Middle East respiratory syndrome coronavirus vaccine based on a recombinant measles virus vaccine platform. J. Virol. *89*, 11654–11667.

Mendlovic, F., Cruz-Rivera, M., Ávila, G., Vaughan, G., and Flisser, A. (2015). Cytokine, antibody and proliferative cellular responses elicited by Taenia solium calreticulin upon experimental infection in hamsters. PLoS One *10*, e0121321.

Moghaddam, A., Olszewska, W., Wang, B., Tregoning, J.S., Helson, R., Sattentau, Q.J., and Openshaw, P.J.M. (2006). A potential molecular mechanism for hypersensitivity caused by formalin-inactivated vaccines. Nat. Med. *12*, 905–907.

Mulisch, M., and Welsch, U. (2015). Romeis - Mikroskopische Technik (Springer Berlin Heidelberg).

Munoz, F.M., Cramer, J.P., Dekker, C.L., Dudley, M.Z., Graham, B.S., Gurwith, M., Law, B., Perlman, S., Polack, F.P., Spergel, J.M., et al. (2021). Vaccine-associated enhanced disease: case definition and guidelines for data collection, analysis, and presentation of immunization safety data. Vaccine *39*, 3053–3066.

Nader, P.R., and Warren, R.J. (1968). Reported neurologic disorders following live measles vaccine. Pediatrics *41*, 997–1001.

Nouailles, G., Wyler, E., Pennitz, P., Postmus, D., Vladimirova, D., Kazmierski, J., Pott, F., Dietert, K., Muelleder, M., Farztdinov, V., et al. (2021). Temporal omics analysis in Syrian hamsters unravel cellular effector responses to moderate COVID-19. Nat. Commun. *12*, 4869.

Nürnberger, C., Bodmer, B.S., Fiedler, A.H., Gabriel, G., and Mühlebach, M.D. (2019). A measles virus-based vaccine candidate mediates protection against Zika virus in an allogeneic mouse pregnancy model. J. Virol. *93*, e01485-18.

Olsen, C.W., Corapi, W.V., Ngichabe, C.K., Baines, J.D., and Scott, F.W. (1992). Monoclonal antibodies to the spike protein of feline infectious peritonitis virus mediate antibody-dependent enhancement of infection of feline macrophages. J. Virol. *66*, 956–965.

Openshaw, P.J. (2001). Potential mechanisms causing delayed effects of respiratory syncytial virus infection. Am. J. Respir. Crit. Care Med. *163*, S10–S13.

Osterrieder, N., Bertzbach, L.D., Dietert, K., Abdelgawad, A., Vladimirova, D., Kunec, D., Hoffmann, D., Beer, M., Gruber, A.D., and Trimpert, J. (2020). Age-dependent progression of SARS-CoV-2 infection in Syrian hamsters. Viruses *12*, 779.

Polack, F.P., Hoffman, S.J., Crujeiras, G., and Griffin, D.E. (2003). A role for nonprotective complement-fixing antibodies with low avidity for measles virus in atypical measles. Nat. Med. *9*, 1209–1213.

Polack, F.P., Teng, M.N., Collins, P.L., Prince, G.A., Exner, M., Regele, H., Lirman, D.D., Rabold, R., Hoffman, S.J., Karp, C.L., et al. (2002). A role for immune complexes in enhanced respiratory syncytial virus disease. J. Exp. Med. *196*, 859–865.

Polack, F.P., Thomas, S.J., Kitchin, N., Absalon, J., Gurtman, A., Lockhart, S., Perez, J.L., Pérez Marc, G., Moreira, E.D., Zerbini, C., et al. (2020). Safety and efficacy of the BNT162b2 mRNA Covid-19 vaccine. N. Engl. J. Med. *383*, 2603–2615.

Ramasamy, M.N., Minassian, A.M., Ewer, K.J., Flaxman, A.L., Folegatti, P.M., Owens, D.R., Voysey, M., Aley, P.K., Angus, B., Babbage, G., et al. (2020). Safety and immunogenicity of ChAdOx1 nCoV-19 vaccine administered in a prime-boost regimen in young and old adults (COV002): a single-blind, randomised, controlled, phase 2/3 trial. Lancet *396*, 1979–1993.

Ruckwardt, T.J., Morabito, K.M., and Graham, B.S. (2019). Immunological lessons from respiratory syncytial virus vaccine development. Immunity *51*, 429–442.

Sadoff, J., Le Gars, M., Shukarev, G., Heerwegh, D., Truyers, C., de Groot, A.M., Stoop, J., Tete, S., van Damme, W., Leroux-Roels, I., et al. (2021). Interim results of a phase 1-2a trial of Ad26.COV2.S Covid-19 vaccine. N. Engl. J. Med. *384*, 1824–1835.

Sahin, U., Muik, A., Derhovanessian, E., Vogler, I., Kranz, L.M., Vormehr, M., Baum, A., Pascal, K., Quandt, J., Maurus, D., et al. (2020). COVID-19 vaccine BNT162b1 elicits human antibody and TH1 T cell responses. Nature *586*, 594–599.

Schülke, S., Burggraf, M., Waibler, Z., Wangorsch, A., Wolfheimer, S., Kalinke, U., Vieths, S., Toda, M., and Scheurer, S. (2011). A fusion protein of flagellin and ovalbumin suppresses the TH2 response and prevents murine intestinal allergy. J. Allergy Clin. Immunol. *128*, 1340–1348.e12.

Schülke, S., Waibler, Z., Mende, M.S., Zoccatelli, G., Vieths, S., Toda, M., and Scheurer, S. (2010). Fusion protein of TLR5-ligand and allergen potentiates activation and IL-10 secretion in murine myeloid DC. Mol Immunol *48*. 341–50.

Stanelle-Bertram, S., Schaumburg, B., Kouassi, N.M., Beck, S., Zickler, M., Beythien, G., Becker, K., Bai, T., Jania, H., Müller, Z., et al. (2020). SARS-CoV-2 induced CYP19A1 expression in the lung correlates with increased aromatization of testosterone-to-estradiol in male golden hamsters. Preprint at Research Square. https://doi.org/10.21203/rs.3.rs-107474/v1.

Stephenson, K.E., Le Gars, M., Sadoff, J., de Groot, A.M., Heerwegh, D., Truyers, C., Atyeo, C., Loos, C., Chandrashekar, A., McMahan, K., et al. (2021). Immunogenicity of the Ad26.COV2.S vaccine for COVID-19. JAMA *325*, 1535–1544.

takano, T., Kawakami, C., Yamada, S., Satoh, R., and Hohdatsu, T. (2008). Antibody-dependent enhancement occurs upon re-infection with the identical serotype virus in feline infectious peritonitis virus infection. J. Vet. Med. Sci. *70*, 1315–1321.

Tomazini, B.M., Maia, I.S., Cavalcanti, A.B., Berwanger, O., Rosa, R.G., Veiga, V.C., Avezum, A., Lopes, R.D., Bueno, F.R., Silva, M.V.A.O., et al. (2020). Effect of dexamethasone on days alive and ventilator-free in patients with moderate or severe acute respiratory distress syndrome and COVID-19: the CoDEX randomized clinical trial. JAMA *324*, 1307–1316.

Tscherne, A., Schwarz, J.H., Rohde, C., Kupke, A., Kalodimou, G., Limpinsel, L., Okba, N.M.A., Bošnjak, B., Sandrock, I., Odak, I., et al. (2021). Immunogenicity and efficacy of the COVID-19 candidate vector vaccine MVA-SARS-2-S in preclinical vaccination. Proc. Natl. Acad. Sci. USA *118*. e2026207118.

Tseng, C.-T., Sbrana, E., Iwata-Yoshikawa, N., Newman, P.C., Garron, T., Atmar, R.L., Peters, C.J., and Couch, R.B. (2012). Correction: immunization with SARS coronavirus vaccines leads to pulmonary immunopathology on challenge with the SARS virus. PLoS One *7*, e35421.

van der Lubbe, J.E.M., Rosendahl Huber, S.K., Vijayan, A., Dekking, L., van Huizen, E., Vreugdenhil, J., Choi, Y., Baert, M.R.M., Feddes-de Boer, K., Izquierdo Gil, A., et al. (2021). Ad26.COV2.S protects Syrian hamsters against

G614 spike variant SARS-CoV-2 and does not enhance respiratory disease. NPJ Vaccines *6*, 39.

Vennema, H., de Groot, R.J., Harbour, D.A., Dalderup, M., Gruffydd-Jones, T., Horzinek, M.C., and Spaan, W.J. (1990). Early death after feline infectious peritonitis virus challenge due to recombinant vaccinia virus immunization. J. Virol. *64*, 1407–1409.

Walsh, E.E., Frenck, R., Falsey, A.R., Kitchin, N., Absalon, J., Gurtman, A., Lockhart, S., Neuzil, K., Mulligan, M.J., Bailey, R., et al. (2020). RNA-based COVID-19 vaccine BNT162b2 selected for a pivotal efficacy study. Preprint at medRxiv. https://doi.org/10.1101/2020.08.17.20176651.

Wan, Y., Shang, J., Sun, S., Tai, W., Chen, J., Geng, Q., He, L., Chen, Y., Wu, J., Shi, Z., et al. (2020). Molecular mechanism for antibody-dependent enhancement of coronavirus entry. J. Virol. *94*, e02015-19.

WHO. (2021). WHO Coronavirus (COVID-19) Dashboard. https://covid19.who.int/. 07.10.2021.

Wu, J.T., Leung, K., and Leung, G.M. (2020). Nowcasting and forecasting the potential domestic and international spread of the 2019-nCoV outbreak originating in Wuhan, China: a modelling study. Lancet *395*, 689–697.

Wu, T., Hu, E., Xu, S., Chen, M., Guo, P., Dai, Z., Feng, T., Zhou, L., Tang, W., Zhan, L., et al. (2021). clusterProfiler 4.0: a universal enrichment tool for interpreting omics data. Innovation *2*, 100141.

Wyler, E., Adler, J.M., Eschke, K., Teixeira Alves, G., Peidli, S., Pott, F., Kazmierski, J., Michalick, L., Kershaw, O., Bushe, J., et al. (2022). Key benefits of dexamethasone and antibody treatment in COVID-19 hamster models revealed by single-cell transcriptomics. Mol. Ther. *30*, 1952–1965.

Yuan, L., Zhou, M., Ma, J., Liu, X., Chen, P., Zhu, H., Tang, Q., Cheng, T., Guan, Y., and Xia, N. (2022). Dexamethasone ameliorates severe pneumonia but slightly enhances viral replication in the lungs of SARS-CoV-2-infected Syrian hamsters. Cell. Mol. Immunol. *19*, 290–292.

Zhu, N., Zhang, D., Wang, W., Li, X., Yang, B., Song, J., Zhao, X., Huang, B., Shi, W., Lu, R., et al. (2020). A novel coronavirus from patients with pneumonia in China, 2019. N. Engl. J. Med. *382*, 727–733.

Zivcec, M., Safronetz, D., Haddock, E., Feldmann, H., and Ebihara, H. (2011). Validation of assays to monitor immune responses in the Syrian golden hamster (Mesocricetus auratus). J. Immunol. Methods *368*, 24–35.

STAR★METHODS

KEY RESOURCES TABLE

REAGENT or RESOURCE	SOURCE	IDENTIFIER
Antibodies		
KPL HRP-conjugated goat anti-hamster IgG	Seracare	Cat#5220-0371
mAb against SARS-CoV nucleocapsid protein	Bussmann et al. (2006)	clone 4F3C4
secondary biotinylated goat anti-mouse Ab	Vector Laboratories	Cat#BA-9200-1.5
mAb against M protein of Influenza A virus	ATCC	clone HB-64
Bacterial and virus strains		
MeV_{vac2}-SARS2-S(H)	Hörner et al. (2020)	N/A
MV_{vac2}-GFP(P)	Malczyk et al. (2015)	N/A
SARS-CoV-2 isolate MUC-IMB1	Böhmer et al. (2020)	GenBank# MT270101.1
Chemicals, peptides, and recombinant proteins		
SARS-CoV-2 (2019-nCoV) Spike S1+S2 ECD-His Recombinant Protein	Sino Biological Europe	Cat#40589-V08B1
SARS-CoV-2 Trimeric Spike (stabilized Spike)	NIBSC	Cat#101007
Rec. Ovalbumin	Schülke et al. (2010)	RefSeq# NM205152
Rec. Flagellin A	Schülke et al. (2010)	RefSeq# X65624
Concanavalin A	Sigma-Aldrich	Cat#11028-71-0
MeV bulk antigens	Virion Serion	Cat#BA102VS-S
Dispase	Corning	Cat#354235
DNAse	AppliChem	Cat#A3778,0100
Collagenase B	Roche	Cat#11088815001
Actinomycin D	Sigma-Aldrich	Cat#A9415-5MG
Aluminum hydroxid (Allhydrogel adjuvant 2%)	InvivoGen	Cat#Vac-alu-250
3-Amino-9-ethyl-carbozole	Sigma-Aldrich	Cat#A5754-10G
Dexamethosone	Bela-pharm	Cat#6933074.00.00
Direktrot 80	Sigma-Aldrich	Cat#365548
Entellan	Sigma-Aldrich	Cat#107060
Papanicolaous solution 1b Hematoxylin S	Sigma-Aldrich	Cat#1.09254
RBC Lysis buffer	Santa Cruz Biotechnology	Cat#sc-296258
RNAscope® Pretreatment Reagents	Bio-Techne	Cat#322330 and 322000
RNAscope® Negative Control Probe	Bio-Techne	Cat#310043
TMB substrate	Invitrogen	Cat#00-4201-56
TRIzol Reagent	Ambion, Thermo Fisher Schientific	Cat#15596026
Critical commercial assays		
Chromium Next Gem Chip G Single Cell Kit	10x genomics	Cat#1000121
Chromium Next Gem Single cell 3' GEM, Library & Gel Bead Kit v3.1	10x genomics	Cat#1000120
Direct-zol RNA MiniPrep kit	Zymo research	Cat#R2052
Hamster IFN-γ ELISpot^{BASIC} kit	MABTECH	Cat#3102-2H
QIAseq FastSelect –rRNA HMR Kit	Qiagen	Cat#334385
RNAscope® 2.5 HD Assay – RED Kit	Bio-Techne	Cat#322360
Superscript III one step RT-PCR system with Platinum Tag Polymerase	Invitrogen	Cat#12574-026

(*Continued on next page*)

Continued		
REAGENT or RESOURCE	SOURCE	IDENTIFIER
Vectastain Elite ABC Kit	Vector Laboratories	Cat#PK6100
Deposited data		
Bulk RNA-seq	This Paper	GEO: GSE195939
scRNA seq data	This Paper	GEO: GSE196938
Experimental models: Cell lines		
Vero (African green monkey kidney)	ATCC	CCL-81
Vero clone E6	ATCC	CRL-1586
Experimental models: Organisms/strains		
Syrian golden hamster (Mesocricetus auratus); HsdHan:AURA	Envigo	Art#8903
Oligonucleotides		
Table S4		
Software and algorithms		
ELI.Analyse V5.0	AE.L.VIS	http://www.aelvis.de
fastp algorithm	Chen et al. (2018)	https://github.com/OpenGene/fastp
CLC Genomics Workbench 21.0.4	QIAGEN	https://digitalinsights.qiagen.com
CellRanger v5.0	10x genomics	https://support.10xgenomics.com/single-cell-gene-expression/software
R packages Seurat v4.0	Hao et al. (2021)	https://satijalab.org/seurat/
DoRothEA v3.12	Holland et al. (2020)	https://saezlab.github.io/dorothea/
GSVA R package	Hänzelmann et al. (2013)	http://bioconductor.org/packages/release/bioc/html/GSVA.html
clusterProfiler R package	Wu et al. (2021)	https://bioconductor.org/packages/release/bioc/html/clusterProfiler.html
Prism 9.2.0	GraphPad Software	http://www.graphpad.com
Original code used in the analysis of the single cell data	This Paper	https://github.com/Berlin-Hamster-Single-Cell-Consortium/Vaccine-associated-enhanced-respiratory-pathology-in-COVID-19-hamsters-after-TH2-biased-immunization
Other		
Lysing Matrix M tubes	MP biosciences	Cat#6923100
J-810 Spectropolarimeter	JASCO	https://www.jasco.de/en
Eli.Scan ELISpot scanner	AE.L.VIS	http://www.aelvis.de
Qubit 4 Fluorimeter	Thermo Fisher	Cat#Q33238
Precellys24 tissue homogenizer	bertin TECHNOLOGIES	Cat#P000669-PR240-A
2100 Bioanalyzer Instrument	Agilent	Part#G2939BA
Novaseq 6000	Illumina	Cat#20013850
NextSeq 550	Illumina	Cat#SY-415-1002
Hamamatsu S60 scanner	Hamamatsu Photonics	Prod#C13210
Chromium Controller	10x Genomics	Prod# 1000204

RESOURCE AVAILABILITY

Lead contact

Lead Contact for requests concerning ressources is Michael D. Mühlebach, email: Michael.Muehlebach@pei.de.

Materials availability

Materials will be available upon request; (recombinant) viruses or plasmids may require filing of materials transfer agreements (MTAs) and compensation for shipment.

Data and code availability

Data and Code used in this study are fully available. Bulk RNA-seq and scRNA-seq data generated in this study were submitted to the NCBI GEO database and can be found under accession number NCBI GEO: GSE195939 and GSE196938, respectively. All original code used in the analysis of the single cell data has been deposited at https://github.com/Berlin-Hamster-Single-Cell-Consortium/Vaccine-associated-enhanced-respiratory-pathology-in-COVID-19-hamsters-after-TH2-biased-immunization. All other data are available in the main text or the supplemental information. Any additional information required to reanalyse the data reported in this paper is available from the lead contact upon request.

EXPERIMENTAL MODEL AND SUBJECT DETAILS

Cells

Vero (African green monkey kidney; ATCC# CCL-81) and Vero clone E6 (ATCC# CRL-1586) cells were purchased from ATCC (Manassas, VA, USA) and cultured in Dulbecco's modified Eagle's medium (DMEM, Sigma Aldrich, Steinheim, Germany) supplemented with 10% fetal bovine serum (FBS; Sigma Aldrich) and 2 mM L-glutamine (L-Gln, Sigma Aldrich). Cell cultures were incubated at 37°C in a humidified atmosphere containing 6% CO_2 up to 30 passages after thawing of the initial stocks to ensure authentication of utilized cell lines.

Viruses

MeV_{vac2}-SARS2-S(H) (Hörner et al., 2020) and MV_{vac2}-GFP(P) (i.e. MV_{vac2}-ATU(P) (Del Valle et al., 2007) with GFP inserted in the ATU (Malczyk et al., 2015) have been described previously. Subsequent passages were generated after $TCID_{50}$ titration of infectious virus according to the method of Kaerber and Spaerman (Kärber, 1931). Stocks were generated by infection of Vero cells at an MOI = 0.03, and viruses in P3 or P4 were used for vaccination experiments. SARS-CoV-2 isolate MUC-IMB1 (Böhmer et al., 2020) was used in passage 3 on Vero-E6 cells after isolation from the patient as described before (Hörner et al., 2020).

Syrian golden hamster animal model

All animal experiments were carried out in compliance with the regulations of German animal protection laws and as authorized by the RP Darmstadt and reported according to the ARRIVE guidelines. Six to 12-weeks old Syrian hamsters (Envigo RMS, Venray, Netherlands) were randomized for age- and sex-matched groups. Male and female hamsters were used in a 1:1 ratio to ensure transferability of results to both sexes, cohort sizes (n = 6) were chosen to ensure statistical validation with an error probability of $p < 0.05$ with a power of 80% conservatively assuming an effect size of 0.8. Animals were vaccinated intraperitonally (i.p.) in a prime-boost schedule (days 0 and 21) with 5×10^5 $TCID_{50}$ of recombinant MeV-derived vaccine virus in 200 μL volume or subcutaneously (s.c.) with 10 μg recombinant SARS-CoV-2 S protein (Cat-No. 40589-V08B1, Sino Biological Europe, Eschborn, Germany) adjuvanted with 500 μg aluminum hydroxide (Allhydrogel adjuvant 2%, vac-alu-250, InvivoGen, San Diego, CA, USA) in 100 μL volume. Blood was drawn on days 0 and 21 or 31. Splenocytes of vaccinated animals were isolated 14 days after second immunization or hamsters were challenge by intranasal application of 4×10^3 $TCID_{50}$ SARS-CoV-2 (isolate MUC-IMB1) in passage 3 in 100 μL volume. Alum+S vaccinated hamsters were divided in two groups: i) a untreated group and ii) a dexamethasone treated one (1 mg/kg body weight twice daily orally or subcutaneously). Animals were euthanized 4 days after infection. Specific sections of each lung were prepared for histology (left lobe), analysis of total RNA (right middle lobe), titration of live virus (right apical lobe), and analysis of transcriptomics by scRNA-Seq (caudal lobe), where applicable.

METHOD DETAILS

CD spectroscopy

The secondary structure of SARS-CoV-2 Spike was analysed using circular dichroism spectroscopy and J-810 spectropolarimeter (JASCO) equipped with a quartz cuvette (0.1 cm). Spectra were recorded at room temperature from 255 nm–185 nm by accumulating 10 runs (bandwidth 1 nm, scanning speed 50 nm/min) using 0.16–0.58 μM protein solutions in 20 mM sodium phosphate buffer pH 8.0.

Bronchoalveolar lavage (BAL)

Lungs from sacrificed hamsters were inflated with 2.5 mL PBS via the trachea. The BAL fluid was collected and cells were harvested by centrifugation (1,200 rpm, 4°C, 5 min). The cell-free fluids were removed and the cells were resuspended in 350 μL TRIzol Reagent (Ambion, Thermo Fisher Scientific).

Virus neutralization test (VNT)

Virus neutralization tests (VNT) were performed as described previously (Hörner et al., 2020). In short, serum samples were diluted in 2-fold series in DMEM. 50 PFU MV_{vac2}-GFP(P) or 100 $TCID_{50}$ SARS-CoV-2 were mixed with diluted serum samples and incubated at 37°C for 1 h. Subsequently, the virus-serum mixture was added to 1×10^4 Vero or Vero E6 cells seeded 3 h before in 96 well plates

(Thermo Fisher Scientific, Ulm, Germany). Cells were incubated for 4 days at 37°C in a humidified atmosphere containing 6% CO_2. Virus neutralizing titers were determined as the reciprocal of the highest serum dilution that completely abrogated infectivity.

Total IgG quantification

0.5 μg MeV bulk antigens (Virion Serion, Würzburg) or 0.25 μg recombinant SARS-CoV-2 S protein were coated in 50 μL/well carbonate buffer (Na_2CO_3 30 mM; $NaHCO_3$ 70 mM; pH 9.6) on Nunc Maxisorp® 96 well ELISA plates (eBioscience). After overnight incubation at 4°C, the plates were washed three times with 200 μL PBS containing 0.1% Tween 20 (w/v) and blocked with 100 μL PBS containing 5% BSA and 0.1% Tween 20 for at least 2 h at ambient temperature. Hamster sera were 5-fold serially diluted in PBS containing 1% BSA and 0.1% Tween 20. 50 μL/well of serum dilutions were used in the assay and the plates were incubated at 37°C for 2 h prior to washing the plates three times using PBS containing 0.1% Tween20. Subsequently, 50 μL/well of HRP-conjugated goat anti-hamster IgG (1:1,000 in PBS containing 1% BSA and 0.1% Tween20; Sera care KPL, Cat. 5220-0371) were added and the plates were incubated for 1 h at room temperature. After washing the plates three times, 100 μL/well TMB substrate (Invitrogen) was added. The reaction was stopped by addition of 50 μL/well 1 N H_2SO_4 and the absorbance at 450 nm (specific signal) and 630 nm (reference wavelength) was measured.

IFN-γ ELISpot analysis

Hamster interferon gamma (IFN-γ) enzyme-linked immunosorbent spot (ELISpot) analysis was performed using the Hamster IFN-γ ELISpot^{BASIC} kit (MABTECH, Nacka Strand, Sweden) in combination with multiscreen immunoprecipitation (IP) ELISpot polyvinylidene difluoride (PVDF) 96-well plates (Merck Millipore, Darmstadt, Germany) according to the manufacturer's instructions. 5×10^5 isolated splenocytes were co-cultured with different stimuli in 200 mL RPMI containing 10% FBS, 2 mM L-Gln, 10 mM HEPES pH 7.4, 50 mM 2-mecaptoethanol and 1% Penicillin-streptomycin. To re-stimulate SARS-CoV-2 specific T cells, isolated splenocytes were cultured with 10 mg/mL recombinant SARS-CoV-2 (2019-nCoV) Spike Protein (S1+S2 ECD, His tag) (Sino biological Europe). Recombinant Ovalbumin [10 mg/mL] served as negative protein control. In parallel, splenocytes were stimulated with 10 mg/ml MeV bulk antigen (Virion Serion, Würzburg, Germany). General stimulation of T cells was achieved using 5 μg/mL concanavalin A (ConA, Sigma-Aldrich) or recombinant 20 μg/mL Flagellin A produced in house (Schülke et al., 2011). Untreated splenocytes served as negative control. After 36 h of stimulation, cells were removed and plates were incubated with biotinylated detection antibodies and Streptavidin-HRP conjugate following the manufactures introductions using a 1 in 100 dilution for the streptavidin-HRP conjugate with 3-Amino-9-ethyl-carbazole (AEC; Sigma-Aldrich) dissolved in N,N-dimethylformamide (Merck Millipore) as substrate. Spots were counted using an Eli.Scan ELISpot scanner (AE.L.VIS, Hamburg, Germany) and analysis software ELI.Analyse V5.0 (AE.L.VIS).

Determination of infectious virus lung titers

The right apical lobe of the lungs of infected animals was snap-frozen in liquid nitrogen and homogenized in 1 mL ice-cold DMEM containing 2 mM L-Gln and 1% Penicillin/Streptomycin in Lysing Matrix M tubes (MP Bioscience, Hilton, UK) using the Precellys24 tissue homogenizer (bertin TECHNOLOGIES, Montigny-le-Bretonneux, France) for 2 × 10 s at 6,000 rpm. Samples were kept on ice at all times. Subsequently, organ debris was removed by centrifugation (13 min, 6,800 rpm, 4°C). Vero E6 cells were inoculated with the supernatants in a 10-fold dilution series for 7 d at 37°C. SARS-CoV-2 organ titers were calculated by the $TCID_{50}$ method of Kaerber and Spearman according to virus-induced CPE and adjusted for 1 g of tissue.

RNA preparation

The right middle lobe of the lungs of infected animals was homogenized in 1 mL TRIzol Reagent (Ambion, Thermo Fisher Scientific) in Lysing Matrix M tubes (MP Bioscience, Hilton, UK) using the Precellys24 tissue homogenizer (bertin TECHNOLOGIES) for 2 × 15 s at 6,000 rpm. Samples were kept on ice at all times. Organ debris was removed by subsequent centrifugation (13 min, 6,800 rpm, 4°C). Clear supernatant was used for RNA purification with Direct-zol RNA MiniPrep kit (Zymo research, Freiburg (Breisgau), Germany) according to the manufactures introduction.

Quantitative reverse-transcription PCR (qRT-PCR)

RNA samples were quantified by quantitative reverse transcription-PCR (qPT-PCR) using Superscript III one step RT-PCR system with Platinum Tag Polymerase (Invitrogen, Darmstadt, Germany). Primer and probe sequences for mRNA encoding the SARS-CoV-2 E gene (Corman et al., 2020), hamster RPL18 (Zivcec et al., 2011), IL-4, and IL-13 (Espitia et al., 2010) were used as described and are indicated in Table S4. Primers for detection of Eoatxin-1 (Stanelle-Bertram et al., 2020) and forward primer sequences for IL-5 (Mendlovic et al., 2015) were ordered as described. The reverse primer sequence for IL-5 was adapted according to RNA Seq results of hamster lungs as described in this manuscript. Probes for mRNA encoding Eotaxin and IL-5 were designed as shown in Table S3. Reactions were run in 96-well plates (Bio-Rad Laboratories, Hercules, CA) using CFX96 qPCR cycler (Bio-Rad Laboratories) and 5 μL RNA in a total reaction volume of 25 μL in triplicates. An internal Hamster reference (linear range, 4.5×10^6 to 4.5×10^2 copies (Hörner et al., 2020)) was used for quantification of SARS-CoV-2 E gene copy numbers. This reference was validated for copy numbers of RPL18 housekeeping gene by utilization of a PCR product DNA reference generated as described (Osterrieder et al., 2020), and was used for quantification in subsequent runs (linear range, 1.8×10^5 to 1.82×10^2 copies). The following cycling conditions were used for all analyses: reverse transcription for 10 min at 55°C, denaturation for 180 s at 94°C, followed by 45 cycles of 15 s at

94°C and 30 s at 58°C. Quantified sample copy numbers were normalized to copy numbers of the hamster housekeeping gene RPL18. If direct quantification was not possible, the ΔΔct method was used.

Total RNA-Seq

The isolated RNA samples were used for NNSR priming based RNA-Seq library preparation (Levin et al., 2010) (as described in (Brown et al., 2020), vRNA NGS section) with the following modifications. Total RNA, was subjected to rRNA removal using the QIAseq FastSelect –rRNA HMR Kit (Qiagen) in combination with reverse transcription as follows. A 35 μL reaction mixture containing 1 μg RNA, 100 pmol NNSR_RT primer (gctcttccgatctctNNNNNN), 8 μL of 5× SuperScript IV buffer (Invitrogen) 20 pmol dNTPs and 1 μL of FastSelect-rRNA mix was subjected to the following hybridization protocol: 75°C 2 min, 70°C 2 min, 65°C 2 min, 60°C 2 min, 55°C 2 min, 37°C 5 min, 25°C 5 min, store at 4°C. For cDNA synthesis the reaction above was supplemented with dithiothreitol (10 mM), 20 U of RiboLock ribonuclease inhibitor (Thermo Fisher Scientific) and 200 U of SuperScript IV reverse transcriptase in a final reaction volume of 40 μL and incubated 45°C 5 min, 70°C 15 min.

The smears of 200–500 base pairs of the final barcoded libraries were purified from a 1.5% agarose gel and sequenced on a NextSeq 550 Illumina instrument using a single-end 86 bp setting. The RNS-Seq library preparation method used results in reads that start with the same two initial nucleotides. Hence, these were removed when performing quality- and minimum length- read trimming with the fastp algorithm (Chen et al., 2018) with the default parameters. Read mapping to the Hamster genome scaffold, statistical analyses of DEGs between groups and GO analyses were performed using CLC Genomics Workbench (QIAGEN).

Isolation of single cells from lung tissue

The right caudal lobe of the lung was removed from the body and transferred on ice in PBS containing 1% BSA (w/v) and 2 mg/mL Actinomycin D (Sigma-Aldrich) for further processing. Lung tissue was incubated in 2 mL Dispase (Corning, Bedford, MA, USA) containing 2 mg DNAse (AppliChem, Darmstadt, Germany), 4.6 mg Collagenase B (Roche, Basel, Switzerland) and 2 mg/mL Actinomycin D (Sigma-Aldrich) and at 37°C for 30 min. Digest was stopped by the addition of cold PBS containing 0.5% (w/v) BSA and Actinomycin D. The tissue was disrupted by pipetting in a repeated pumping motion. Cell suspension was collected and filtered through 70 mm-filter to obtain a single-cell suspension. Red Blood cell were lysed by incubation with RBC lysis buffer (Santa Cruz Biotechnology, Dallas, Texas, USA) for 4 min at room-temperature. Lysis reaction as stopped by the addition of PBS containing 0.04% BSA, the supernatant was removed by centrifugation (1,200 rpm, 6 min, 4°C) and cells were resuspended in PBS containing 0.04% BSA. Barcoding of single cells and RNA isolation was performed using the Chromium controller and Chromium Next Gem Chip G Single Cell Kit and Chromium Next Gem Single cell 3′ GEM, Library & Gel Bead Kit v3.1 (10x Genomics B.V., Leiden, The Netherlands) according to the manufactures instructions.

Single-cell RNA-Seq

After enzymatic fragmentation and size selection, resulting double-stranded cDNA amplicons optimized for library construction were subjected to adaptor ligation and sample index PCRs needed for Illumina bridge amplification and sequencing according to the manufacturer's instruction (10x genomics). Single cell libraries were quantified using Qubit (Thermo Fisher) and quality-controlled using the Bioanalyzer System (Agilent). Sequencing was performed on a Novaseq 6000 (Illumina), aiming for 200 Million reads per library (read1: 28, read2: 150 nucleotides). Data were analysed using CellRanger v5.0 (10x Genomics) using hamster and SARS-CoV-2 genome scaffolds, and the R packages Seurat v4.0 (Hao et al., 2021) and DoRothEA v3.12 (Holland et al., 2020) were used for cell clustering, annotation, and transcription factor activity analysis. Median gene number detected per cell ranged between 2000 and 4400, with 3800–18500 median UMI counts per cell. Gene set variation analysis (GSVA) was performed using the GSVA R package (Hänzelmann et al., 2013) and gene set enrichment analysis was performed using the clusterProfiler R package (Wu et al., 2021).

Histopathology

The left lung lobe was carefully removed and immersion-fixed in 10% neutral-buffered formalin for 7 days. The tissue was subsequently paraffin-embedded and sections of 4 μm were prepared.

Hematoxilin-eosin staining

Hematoxylin-eosin staining was carried out in accordance with standard procedures (Mulisch and Welsch, 2015). H&E stained slices were subjected to histopathologic analyses on blinded samples.

Sirius red staining

For Sirius Red staining of lung tissue sections we followed the protocol published by Llewellyn with some modifications (Llewellyn, 1970). Briefly, sections were placed in Papanicolaous solution 1b Hematoxylin S (Sigma Aldrich) for 2 min and rinsed afterwards with water followed by ethanol, 3% HCl in ethanol and 70% ethanol. Subsequently, sections were stained for 90 min in alkaline Sirius red (0.5 g Direktrot 80, Sigma in 50% ethanol containing 0.1‰ NaOH) before rinsing with water. Sections were dehydrated afterwards with increasing ethanol concentrations and xylene. Finally, sections were covered with Entellan (Merck KGaA, Darmstadt, Germany).

In situ *hybridisation*

To detect viral RNA in the lungs, fixed paraffin-embedded tissue sections were mounted on glass slides and analyzed by *in situ* hybridization as described previously (Halwe et al., 2021; Tscherne et al., 2021). For this, the RNAscope® 2.5 HD Assay – RED Kit (Bio-Techne, cat. no. 322360) was used according to the manufacturer's instructions. Slides were incubated at 60°C, deparaffinized with

xylene and 100% ethanol and pretreated with RNAscope® Pretreatment Reagents (cat. no. 322330 and 322000), to enable access to the target RNA. Subsequently, the RNA-specific probe, targeting the S protein of the SARS-CoV-2 virus (cat. no. 848561) was hybridized to the RNA. After the amplification steps, Fast Red substrate was administered to the samples for signal detection. Slides were counterstained with Gill's Hematoxylin I and 0.02% ammonia water. A RNAscope® Negative Control Probe (cat. no. 310043) was used in parallel to control background staining.

Immunohistochemistry

For SARS-CoV-2 antigen detection, a monoclonal Ab against the nucleocapsid protein (clone 4F3C4 (Bussmann et al., 2006)) was used according to standardized procedures of avidin-biotin-peroxidase complex-method (ABC, Vectastain Elite ABC Kit, Burlingame, CA, USA). Briefly, 2–3 μm sections were mounted on adhesive glass slides, dewaxed in xylene, followed by rehydration in descending graded alcohols. Endogenous peroxidase was quenched with 3% hydrogen peroxide in distilled water for 10 min at room temperature. Antigen heat retrieval was performed in 10 mM citrate buffer (pH 6) for 20 min in a pressure cooker. Nonspecific Ab binding was blocked for 30 min at room temperature with goat normal serum, diluted in PBS (1:2). The primary Ab was applied overnight at 4°C (1:50, diluted in TRIS buffer), the secondary biotinylated goat anti-mouse Ab was applied for 30 min at room temperature (Vector Laboratories, Burlingame, CA, USA, 1:200). Color was developed by incubating the slides with freshly prepared avidin-biotin-peroxidase complex (ABC) solution (Vectastain Elite ABC Kit; Vector Laboratories), followed by exposure to 3-amino-9-ethylcarbazole substrate (AEC, Dako, Carpinteria, CA, USA). The sections were counterstained with Mayer's haematoxylin and coverslipped. As negative control, consecutive sections were labelled with an irrelevant Ab (M protein of Influenza A virus, ATCC clone HB-64). A positive control slide was included in each run. Slides were scanned using a Hamamatsu S60 scanner (Hamamatsu Photonics, K.K. Japan).

QUANTIFICATION AND STATISTICAL ANALYSIS

Animal cohort or sample size per treatment was between n = 4 and n = 6 as defined in the individual figure legends. Statistical analysis of different experiments is indicated in detail in the respective figure legends. For statistical analysis of samples from animal experiments, ordinary one-way or two-way ANOVA was applied with Tukey's multiple comparisons test using Prism. For statistical analysis of grouped ELISpot data, paired t test was applied using Prism. For statistical analysis of histopathology, ordinary one-way ANOVA was applied with Mann-Whitney test. For statistical analysis of qRT-PCR analyses, ordinary one-way ANOVA was applied with Tukey's multiple comparisons test using Prism.

Bulk RNAseq libraries from different hamster lungs (n = 4) were generated for each condition (mock uninfected, infected, Alum+S vaccinated + infected, and MeV_{vac2}-SARS2-S(H) vaccinated + infected). An average of 13,400,912.5 (range 8,468,387 to 22,180,134) reads mapped to the hamster genome scaffold MesAur1.0.102, an average of 90.1% (range 87.95%–92.04%) of the total number of reads, with 98.7% (range 97.61%–99.27%) representing protein-coding segments. An average 62,455.9 (range 2,649 to 205,001) reads mapped to SARS-CoV-2 reference genome (NCBI accession #LR824570), about 0.41% (range 0.03%–1.25%) of the total number of reads. For statistical comparison, read counts of libraries of vaccinated animals were tested against mock animals using CLC Genomics Workbench 21.0.4 employing multi-factorial statistics based on a negative binomial Generalized Linear Model (GLM). p-values of differentially expressed genes (DEG) were corrected with FDR correction method.

Four scRNA-seq libraries from four different infected hamster lungs were generated for each condition (mock, Alum+S vaccinated, and MeV_{vac2}-SARS2-S(H) vaccinated) and an average number of 2,679 cells (range: 1,392 to 4,645) were retrieved per library with an average read count of 7,271 mapped reads per cell. Differential expression of selected cytokines in different celltype compartments between treatment groups was performed using the FindMarkers function from the Seurat R package with the default parameters (Wilcoxon Rank Sum test with Bonferroni p value correction).

Differential expression of SARS-CoV-2 RNA in scRNA-Seq experiments was analysed using the Loupe Browser 6.0.0 software. Statistical significance was tested by comparison of individual cell populations with all other cells within the different treatment groups, p values were adjusted using Benjamini-Hochberg correction for multiple testings.

We did not determine by statistical tests whether the data met assumptions of the statistical approach, also for the reason that tests were conservatively chosen for data requirements to have to meet as few pre-assumptions as possible.

Cell Reports, Volume *40*

Supplemental information

Vaccine-associated enhanced respiratory pathology in COVID-19 hamsters after T_H2-biased immunization

Aileen Ebenig, Samada Muraleedharan, Julia Kazmierski, Daniel Todt, Arne Auste, Martina Anzaghe, André Gömer, Dylan Postmus, Patricia Gogesch, Marc Niles, Roland Plesker, Csaba Miskey, Michelle Gellhorn Serra, Angele Breithaupt, Cindy Hörner, Carina Kruip, Rosina Ehmann, Zoltan Ivics, Zoe Waibler, Stephanie Pfaender, Emanuel Wyler, Markus Landthaler, Alexandra Kupke, Geraldine Nouailles, Christine Goffinet, Richard J.P. Brown, and Michael D. Mühlebach

Figure S1. Relative secondary structural elements of S determined by circular dichroism (CD), Related to Figure 1

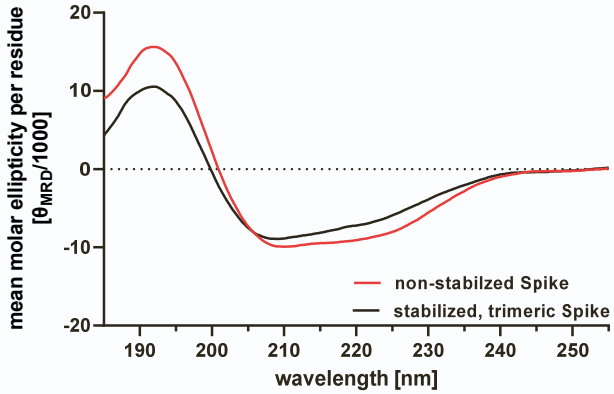

Suppl. Fig. S1: Relative secondary structural elements of S determined by circular dichroism (CD). To determine misfolding of recombinant Spike used for vaccination, spectra of non-stabilized recombinant S used for vaccination (red; Sino Biological, Cat.-No. 40589-V08B1) and soluble S stabilized in the native conformation (black; NIBSC, Cat.-No. 101007), secondary structure of the proteins was determined by CD spectroscopy. CD spectra of both proteins were recorded at room temperature from 255 nm – 185 nm by accumulating 10 runs, blotted and analysed for relative content of α-helical and β-sheet secondary structural elements.

Figure S2. Eosinophil infiltration into tissue of infected hamster lungs. Related to Figure 1

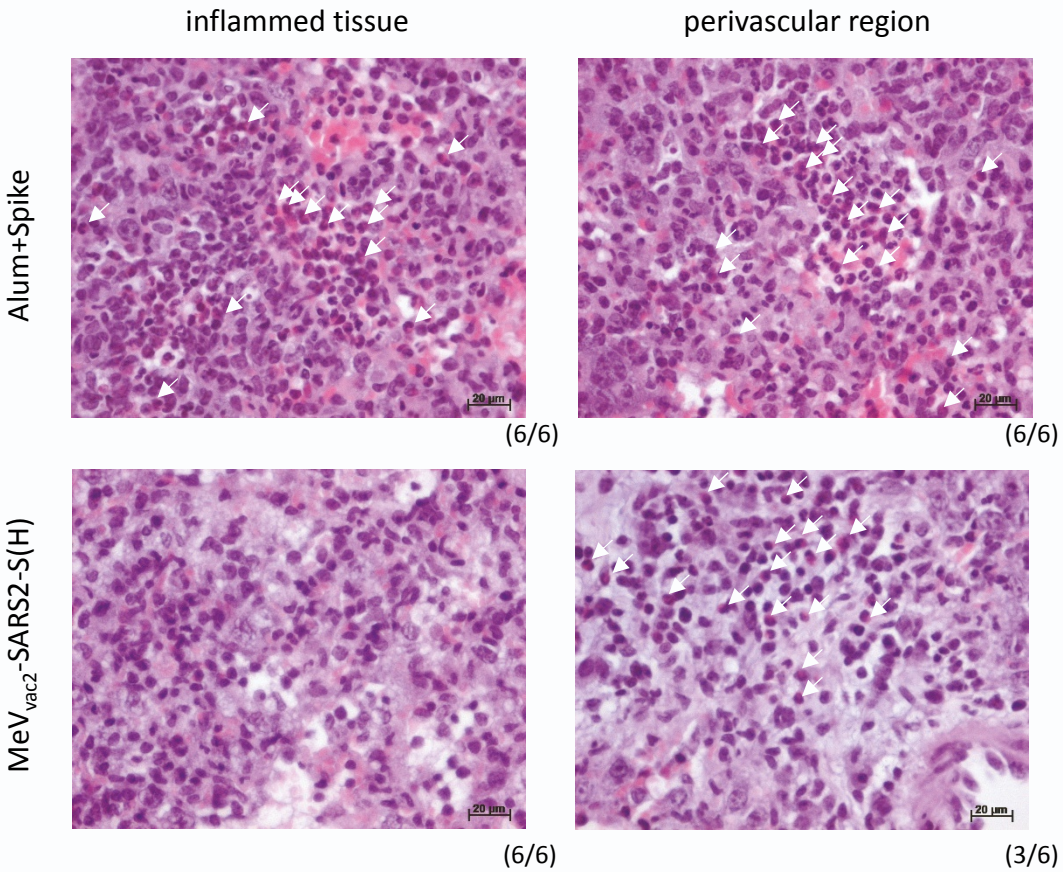

Suppl. Fig. S2: Eosinophil infiltration into tissue of infected hamster lungs. Haematoxilin and Eosin-staining of fixed lung slices of hamsters infected with SARS-CoV-2 after vaccination with Aluminum-adjuvanted Spike protein (upper panel) or MeV$_{vac2}$-SARS2-S(H) (lower panel) revealed eosinophil infiltration into inflammed tissue (left panel) of Alum+S, but not MeV$_{vac2}$-SARS2-S(H) immunized animals´. While eosinophils became evident in the perivascular region of samples of all animals vaccinated with protein before infection, only half (3/6) of the MeV-vaccinated animals revealed this phenotype. N = 6; representative pictures for the fraction of animals indicated below each picture. White arrows depict single eosinophils. Scale bar, 20 µm.

Figure S3. : Induction of α-SARS-CoV-2 S and α-MeV specific antibodies. Related to Figure 4

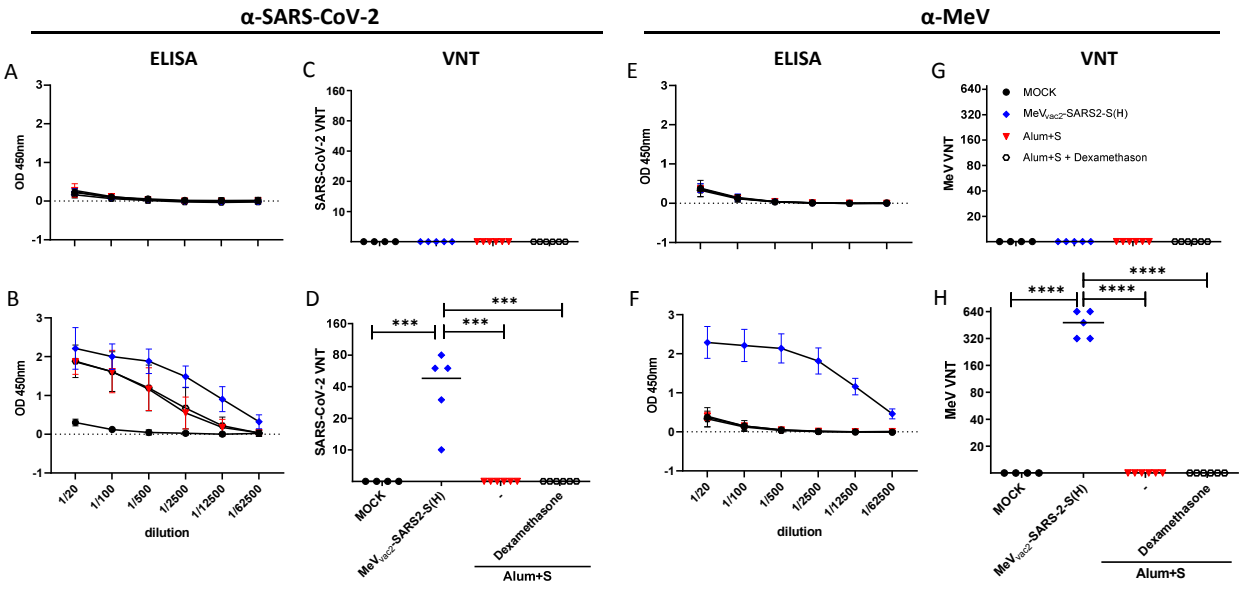

Suppl. Fig. S3: Induction of α-SARS-CoV-2 S and α-MeV specific antibodies. Sera of hamsters vaccinated on days 0 and 21 with MeV$_{vac2}$-SARS2-S(H) (blue diamonds) or Alum-adjuvanted S protein (red triangles, open circles) were collected on days 0 (A, C, E, G) and 31 (B, D, F, H) and analyzed for antibodies specific for SARS-CoV-2 S or MeV. Medium-inoculated hamsters (black circles) served as mock. Pan-IgG binding to recombinant SARS-CoV-2 S (A, B) or MeV bulk antigen (E, F) were determined by ELISA via the specific OD 450 nm value. Depicted are means and the respective standard deviation of each group (n = 4 - 6). Virus-neutralizing titers (VNT) in vaccinated hamsters for SARS-CoV-2 (C, D) or MeV (G, H) were calculated as the reciprocal of the highest dilution abolishing infectivity. For statistical analysis, ordinary one-way ANOVA was applied with Tukey's multiple comparisons test. ns, not significant ($p>0.05$), *, $p<0.05$; **, $p<0.01$;***, $p<0.001$;****, $p<0.0001$.

Figure S4. Gross pathology in vaccinated hamsters after challenge. Related to Figure 4

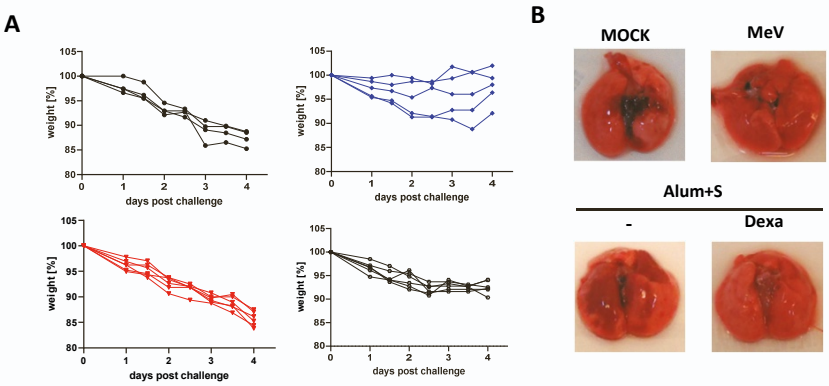

Suppl. Fig. S4: Gross pathology in vaccinated hamsters after challenge. Hamster were vaccinated at days 0 and 21 and challenged on day 35 with low-passage SARS-CoV-2. **(A)** Body weight changes of animals vaccinated with medium (upper left, black circles), MeV_{vac2}-SARS2-S(H) (upper right, blue diamonds), Alum+S without (lower left, red triangles) or with dexamethasone-treatment after challenge (lower right, open circles). **(B)** Macroscopic pathology of Syrian hamster lungs after SARS-CoV-2 infection and indicated vaccination or treatment on day 4 pi.

Figure S5. Deregulation of T_H2 cytokines in lungs (A) and BAL cells (B) of SARS-CoV-2 infected, vaccinated Syrian hamsters 4 dpi. Related to Figure 5.

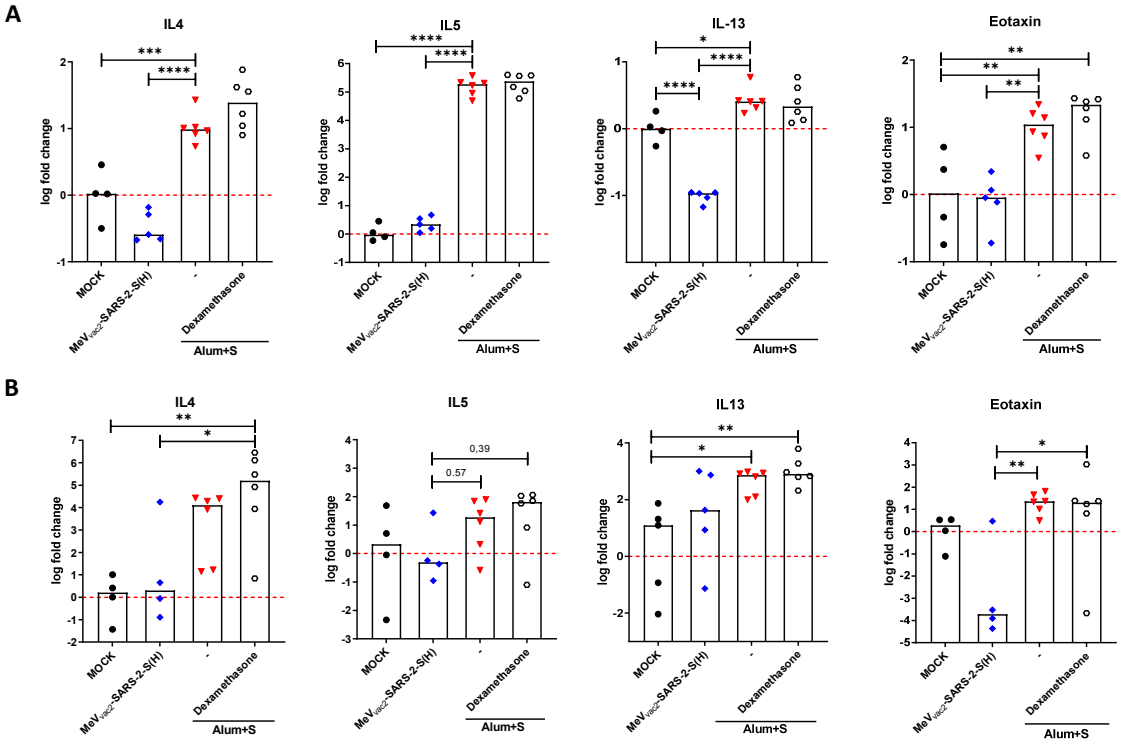

Suppl. Fig. S5: Deregulation of T_H2 cytokines in lungs (A) and BAL cells (B) of SARS-CoV-2 infected, vaccinated Syrian hamsters 4 dpi. Depicted are data of animals already displayed in Fig. 4**.** Relative fold-change expression of mRNAs encoding IL-4, IL-5, or IL-13 was determined using quantitative RT-PCR and the ΔΔct method. mRNA encoding RPL18 was used as housekeeping gene for normalization. Median of samples from mock-treated hamsters served as reference to normalize relative gene expression. Dots represent individual animals; mock-vaccinated hamsters, black circles; MeV$_{vac2}$-SARS2-S(H)-vaccinated hamsters, blue diamonds; protein-vaccinated hamsters, red triangles. For statistical analysis, ordinary one-way ANOVA was applied with Tukey's multiple comparisons test. ns, not significant (p>0.05), *, p<0.05; **, p<0.01;***, p<0.001;****, p<0.0001.

Figure S6. SARS-CoV-2 infection triggers cell-type specific induction of REACTOME pathways which differ depending on vaccination type and prior immune status. Related to Figure 6.

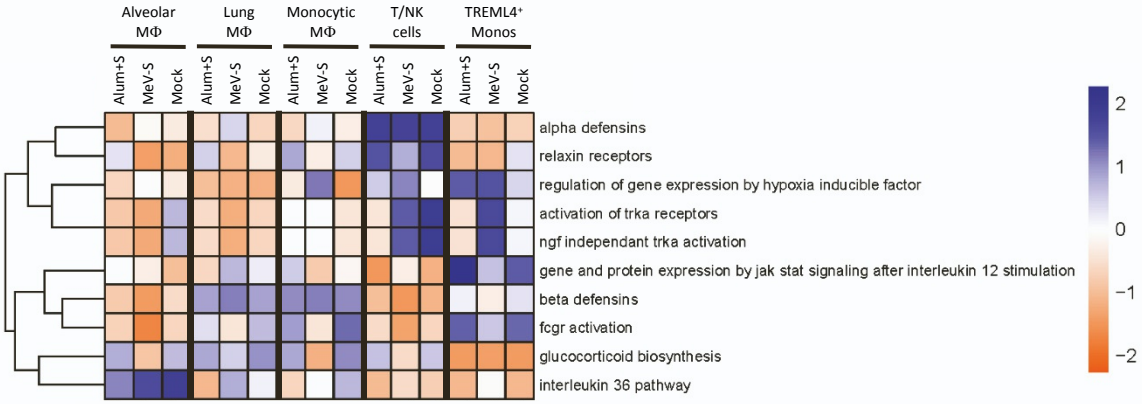

Suppl. Fig. S6: SARS-CoV-2 infection triggers cell-type specific induction of REACTOME pathways which differ depending on vaccination type and prior immune status. Heat map is derived from scRNA-seq data and highlights selected REACTOME pathways which exhibit differential activation or suppression triggered by infection. Differences are dependent on prior immune status or vaccination type, and are cell-type specific. Cell population specific activation or suppression of pathways observed in alveolar macrophages (MΦ), interstitial macrophages, monocytic macrophages, Treml4^{+} monocytes, and T/NK cells is presented. Heat map is colored relative to the activation z-score gradient presented in the scale bar**.**

Figure S7. SARS-CoV-2 infection induces cell-type specific enrichment of GO terms and activation or suppression of KEGG pathways, which differ dependent on prior vaccination type. Related to Figure 6.

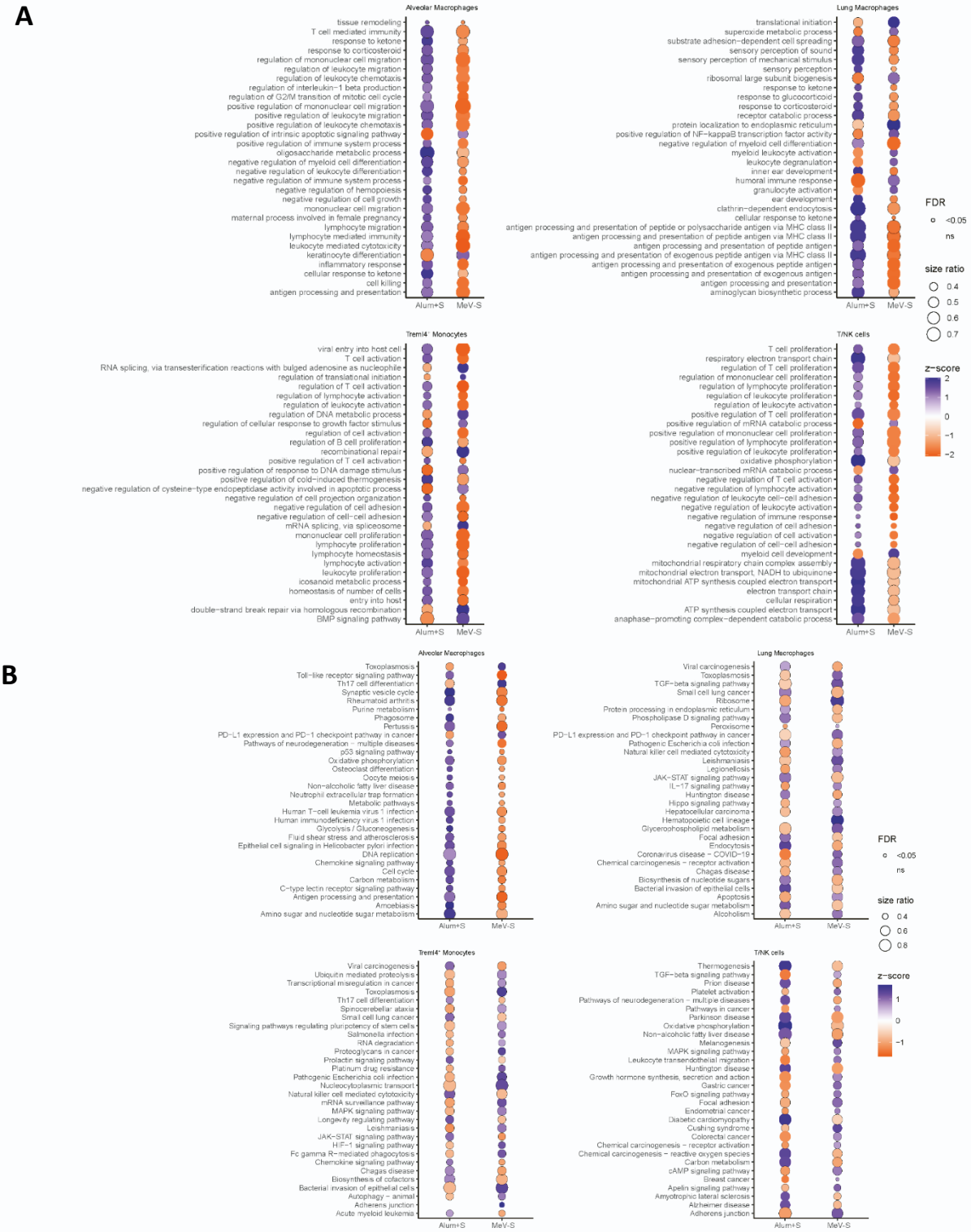

Suppl. Fig. S7: SARS-CoV-2 infection induces cell-type specific enrichment of GO terms and activation or suppression of KEGG pathways, which differ dependent on prior vaccination type. Dot plots highlight enriched (A) GO categories or (B) KEGG pathways that exhibit differential activation status dependent on prior vaccination with either Alum+S or MeVvac2-SARS2-S(H). Individual comparison plots are derived from scRNA-seq data and represent differential enrichment observed in alveolar macrophages, interstitial macrophages, Treml4^{+} monocytes and T/NK cells. Enriched categories are labelled on the y-axes. Circle size represents the ratio of significantly dysregulated genes relative to the total gene number in a specific GO term or KEGG pathway. Circles are colored relative to activation z-score gradient presented in the scale bar, with significantly enriched categories or pathways (FDR $p<0.05$) highlighted with a black boarder. ns: non-significant

Table S1. Histopathological analysis of lung tissue of vaccinated Syrian hamsters batch #1 upon challenge with SARS-CoV-2. Related to Figure 1. Hamsters were vaccinates with medium (MOCK), MV_{vac2}-ATU(P) as measles-only vector control (MeV), MeV_{vac2}-SARS2-S(H) (MeV-S), or Alum-adjuvanted Spike protein (Alum+S). The left lobe of vaccinated hamster lungs was dissected 4 dpi. H& E staining revealed histopathological changes and immune cell infiltration assessed by a trained pathologist in a blinded manner. DIC, disseminated intravascular coagulation.

Animal-No.	Vaccine group	% Dense Area	Bronchia	Vessels	DIC	Dense Area	Fibrosis	Syncytia
47	MOCK	< 50% dense areas, clearly bronchial-associated	Marked purulent bronchitis (granulocytes and lymphocytes in the lumen), bronchial epithelium sometimes with inflammatory infiltration.	Vascular walls with inflammatory infiltration, Single-cell necrosis in the vessel wall, multiple hemorrhages in the tissue, 2 x edema around vessels	No	mostly lymphocytes and macrophages, less with granulocytes, sporadic eosinophils, proliferation of type II pneumocytes, often karyorrhexis	No	No
48	MOCK	30% dense areas, Bronchial- and vessel- associated	Bronchitis (lymphocytes and only very few granulocytes in the lumen), bronchial epithelium with little inflammatory infiltration and damage.	Vascular walls with inflammatory infiltration, Single-cell necrosis in the vessel wall, no bleeding or edema	No	mostly lymphocytes, macrophages, pneumocytes, isolated eosinophils, often karyorrhexis	No	No
49	MOCK	approximately 50% dense areas, clearly bronchial-associated	Bronchitis (lymphocytes and granulocytes in the lumen), bronchial epithelium sporadically with inflammatory infiltration, little damage.	Vascular walls with inflammatory infiltration, multiple hemorrhages in the tissue, 2 x edema around vessels	No	mostly lymphocytes, macrophages, pneumocytes, no granulocytes, eosinophils not increased, Foci with massive karyorrhexis	No	No
50	MOCK	approximately 33% dense areas, clearly bronchial-associated	Bronchitis (lymphocytes and granulozytes in the lumen), bronchial epithelium with little inflammatory infiltration and damage (karyorrhexis).	Vascular walls with inflammatory infiltration (also eosinophils), multiple hemorrhages in the tissue, 2 x edema around vessels	No	mostly lymphocytes, macrophages, pneumocytes, isolated eosinophils, foci with karyorrhexis	No	No
51	MOCK	approximately 33% dense areas, clearly bronchial-associated	Bronchitis (lymphocytes and granulocytes in the lumen), bronchial epithelium sporadically with inflammatory infiltration, little damage.	Vascular walls with inflammatory infiltration (also eosinophils), multiple hemorrhages in the tissue, 2 x edema around vessels	No	mostly lymphocytes, macrophages, pneumocytes, isolated eosinophils, frequent karyorrhexis	No	No
52	MOCK	approximately 33% dense areas (macroscopic), bronchial- and vessel-associated, diffuse distribution	Bronchitis (only few lymphocytes and granulocytes in the lumen) bronchial epithelium with inflammatory infiltration, little damage	Vascular walls with inflammatory infiltration, clear single cell necrosis in the vessel wall, several hemorrhages in the tissue.	No	diffused distributed, mostly lymphocytes, macrophages, pneumocytes, Isolated eosinophils, frequent karyorrhexis	No	No
53	Alum+S	approximately 33% dense areas (macroscopic), bronchial- and vessel-associated, diffuse distribution	Bronchitis (only few lymphocytes, granulocytes and little karyorrhexis in the lumen) bronchial epithelium with little inflammatory infiltration, marked proliferation of the bronchial epithelium, clear damage	Vessel walls only sporadically infiltrated with inflammation, hemorrhages in the tissue	No	mostly lymphocytes, macrophages, pneumocytes, massive eosinophils, frequent karyorrhexis	No	No

Animal-No.	Vaccine group	% Dense Area	Bronchia	Vessels	DIC	Dense Area	Fibrosis	Syncytia
54	Alum+S	30% dense areas, bronchial- and vessel-associated	Bronchitis (lymphocytes and granulocytes in the lumen), bronchial epithelium: foci of inflammatory infiltration, marked proliferation of the bronchial epithelium,clear damage	Vessel walls only very slightly infiltrated, several hemorrhages in the tissue.	No	mostly lymphocytes, macrophages, pneumocytes, massive eosinophils, frequent karyorrhexis	No	Yes
55	Alum+S	40% dense areas, not bronchial- or vessel- associated	Bronchitis (Lymphocytes and granulocytes in the lumen), bronchial epithelium: foci of inflammatory infiltration, marked proliferation of the bronchial epithelium, clear damage	Vascular walls with inflammatory infiltration, significant single cell necrosis in the vascular wall, 1 x hemorrhages in the tissue, 1 x edema around vessels.	No	mostly lymphocytes, macrophages, pneumocytes, massive eosinophils, frequent karyorrhexis	No	Suspicion
56	Alum+S	80% dense areas, not clearly bronchial or vessel associated.	Bronchitis (lymphocytes and granulocytes in the lumen), bronchial epithelium: foci of inflammatory infiltration, marked proliferation of the bronchial epithelium, clear damage	Vascular walls with inflammatory infiltration, isolated single cell necrosis in the vascular wall, multiple hemorrhages in tissue, slight edema around vessels.	No	mostly lymphocytes, macrophages, pneumocytes, massive eosinophils, only sporadic karyorrhexis	No	No
57	Alum+S	50% dense areas, not clearly bronchial or vessel associated.	Bronchitis (lymphocytes, granulocytes and karyorrhexis in the lumen), bronchial epithelium with very little inflammatory infiltration, no karyorrhexis, little damage	Vascular walls with inflammatory infiltration, isolated single cell necrosis in the vascular wall, sporadic hemorrhages in the tissue.	No	mostly lymphocytes, macrophages, pneumocytes, massive eosinophils, only sporadic karyorrhexis	No	No
58	Alum+S	40% dense areas, not clearly bronchial or vessel associated.	Bronchitis (lymphocytes, granulocytes and karyorrhexis in the lumen), bronchial epithelium: Foci of inflammatory infiltration, very few karyorrhexis, little damage	Vascular walls with inflammatory infiltration, 1 x single cell necrosis in the vascular wall, 2 x hemorrhages in the tissue.	No	mostly lymphocytes, macrophages, pneumocytes, massive eosinophils, only sporadic karyorrhexis	No	No
59	MeV	50% dense areas, not clearly bronchial or vessel associated, diffuse distribution	Bronchitis (lymphocytes, granulocytes and karyorrhexis in the lumen), bronchial epithelium with focal inflammatory infiltration, no karyorrhexis, little damage	Vascular walls with inflammatory infiltration, sporadic single cell necrosis in the vascular wall, multiple hemorrhages in the tissue.	No	mostly lymphocytes, macrophages, pneumocytes, few eosinophils, more neutrophils	No	No
61	MeV	40% dense areas, bronchial associated, diffuse distribution	Bronchitis (lymphocytes, granulocytes and karyorrhexis in the lumen), bronchial epithelium: foci of inflammatory infiltration, no karyorrhexis, little damage	Vascular walls with inflammatory infiltration, sporadic single cell necrosis in the vascular walls, edema around the vascular wall, multiple hemorrhages in the tissue.	No	mostly lymphocytes, macrophages, pneumocytes, no eosinophils, more neutrophils sporadic karyorrhexis	No	No

Animal-No.	Vaccine group	% Dense Area	Bronchia	Vessels	DIC	Dense Area	Fibrosis	Syncytia
62	MeV	approximately 20% dense areas (macroscopical), bronchial and vessel associated, diffuse distribution	Bronchitis (lymphocytes, granulocytes and karyorrhexis in the lumen), Bronchial epithelium: foci of inflammatory infiltration, no karyorrhexis, little damage	Vascular walls with inflammatory infiltration, sporadic single cell necrosis in the vascular walls, multiple hemorrhages in the tissue.	No	mostly lymphocytes, macrophages, pneumocytes, eosinophile involved, sporadic karyorrhexis	No	No
63	MeV	50% dense areas, not clearly bronchial or vessel associated, diffuse distribution	Bronchitis (lymphocytes and karyorrhexis in the lumen), bronchial epithelium: foci of inflammatory infiltration, sporadic karyorrhexis, proliferation?	Vascular walls with inflammatory infiltration, sporadic single cell necrosis in the vascular walls, edema around the vascular walls, several hemorrhages in the tissue.	No	mostly lymphocytes, macrophages, pneumocytes, eosinophile involved, sporadic karyorrhexis	No	No
64	MeV	60% dense areas, not clearly bronchial or vessel associated, diffuse distribution	Bronchitis (little in the lumen), bronchial epithelium with focal inflammatory infiltration, proliferation?	Vascular walls with inflammatory infiltration (especially veins), several hemorrhages in the tissue.	No	mostly lymphocytes, macrophages, pneumocytes, no eosinophils, sporadic karyorrhexis	No	No
65	MeV-S	20% dense areas (microscopic), clearly bronchial associated	Bronchitis (little in the lumen), bronchial epithelium hardly affected.	Vascular walls with very little inflammatory infiltration, 2 x hemorrhages in the tissue.	No	mostly lymphocytes, macrophages, pneumocytes, isolated eosinophils, no karyorrhexis (1 x ?)	No	No
66	MeV-S	10% dense areas, clearly bronchial associated	Bronchitis (little in the lumen), bronchial epithelium hardly affected.	Vascular walls without inflammatory infiltration, several hemorrhages in the tissue.	No	mostly lymphocytes, macrophages, pneumocytes, isolated eosinophils, sporadic karyorrhexis	No	No
67	MeV-S	25% dense areas, clearly bronchial associated	Mild bronchitis (mostly little in the lumen), bronchial epithelium with sporadic inflammatory infiltration, otherwise not affected.	Vascular walls with infiltration of eosinophils, several hemorrhages in the tissue.	No	mostly lymphocytes, macrophages, pneumocytes, massive eosinophils around vessels, no karyorrhexis	No	No
68	MeV-S	50% dense areas, clearly bronchial-associated	Mild bronchitis (mostly little in the lumen), bronchial epithelium with focal inflammatory infiltration otherwise not affected.	Vascular walls infiltration of eosinophils, several hemorrhages in the tissue.	No	mostly lymphocytes, macrophages, pneumocytes, massive eosinophils around vessels, no karyorrhexis	No	No
69	MeV-S	30% dense areas, clearly bronchial associated	Mild bronchitis (lymphocytes and karyorrhexis in the lumen), bronchial epithelium with focal inflammatory infiltration, significant damage to the bronchial epithelium	Vascular walls with inflammatory infiltration, karyorrhexis in the vascular wall, edema around vessels, massive hemorrhage in the tissue.	No	mostly lymphocytes, macrophages, pneumocytes, significant amount of eosinophils, foci with karyorrhexis	No	Yes
70	MeV-S	60% dense areas, not clearly bronchial associated	Mild bronchitis (lymphocytes, karyorrhexis in the lumen), bronchial epithelium with focal inflammatory infiltration; significant damage to the bronchial epithelium.	Vascular walls with inflammatory infiltration, edema in the vascular wall, edema around the vessels, massive hemorrhages in the tissue.	No	mostly lymphocytes, macrophages, pneumocytes, isolated eosinophils, sporadic karyorrhexis	No	No

Table S2. Histopathological analysis of lung tissue of vaccinated Syrian hamsters batch #2 upon challenge with SARS-CoV-2. Related to Figure 4. Hamsters were vaccinates with medium (MOCK), MV_{vac2}-ATU(P) as measles-only vector control (MeV), MeV_{vac2}-SARS2-S(H) (MeV-S), or Alum-adjuvanted Spike protein (Alum+S). The left lobe of vaccinated hamster lungs was dissected 4 dpi. H& E staining revealed histopathological changes and immune cell infiltration assessed by a trained pathologist in a blinded manner. DIC, disseminated intravascular coagulation**.**

Animal-No.	Vaccine group	% Dense Area	Bronchia	Vessels	DIC	Dense Area	Fibrosis	Syncitia
#93	MOCK	about 30% dense areas, mostly bronchial associated	Bronchial epithelium with inflammatory infiltration, granulocytes in the lumen, partial erythrocytes, some bronchial epithelium in the surrounding tissue	Vascular walls sporadically infiltrated with inflammation, marked hemorrhages	No	few densed areas infiltrated with macrophages, pneumocytes, lymphocytes and granulocytes, no eosinophils, moderate karyorrhexis	No	No
#98	MOCK	max. 10%, small foci, not bronchial associated	slightly altered; low inflammatory infiltration, some inflammatory cells in the lumen	prominent endothelium, minor hemorrhage	No	with increased eosinophils; macrophages and lymphocytes	No	No
#105	MOCK	max. 10%, in a single condensed area, not bronchial associated	slightly altered; low inflammatory infiltration underneath the epithelium	prominent endothelium, minor hemorrhage	No	1 x dense area with macrophages and lymphocytes, hardly any granulocytes, no eosinophils. moderate karyorrhexis.	No	No
#109	MOCK	about 30%, dense areas not clearly bronchial associated	slightly altered; epithelium sporadically with inflammatory infiltration; granulocytes in the lumen	prominent endothelium, hemorrhage	No	Macrophages, pneumocytes, lymphocytes, hardly any granulocytes and eosinophils. Isolated foci with karyorrhexis.	No	No
#113	MOCK	max. 10%, in a single condensed area,	Epithelium clearly altered; scattered inflammatory infiltration, no granulocytes in the lumen	prominent endothelium, significant bleeding	No	Macrophages, pneumocytes, lymphocytes, hardly any granulocytes and eosinophils. Isolated foci with karyorrhexis.	No	No
#91	MeV-S	max. 10%, clear relation to bronchi.	Marked proliferation of the epithelium into the surrounding tissue. Epithelium with inflammatory infiltration	Prominent endothelium, minor hemorrhage?	No	Some eosinophils around vessels, macrophages, pneumocytes, lymphocytes and granulocytes, hardly any karyorrhexis.	No	No
#95	MeV-S	10% dense areas, small multiple foci, bronchial associated	Epithelium not signifiantly altered.	Prominent endothelium, scattered karyorrhexis in vessel walls, only 1 x hemorrhage	No	Some eosinophils in dense area, macrophages, pneumocytes, lymphocytes and granulocytes, hardly any karyorrhexis,	No	No
#99	MeV-S	minimal; only 3 small foci, strictly bronchial associated	Epithelium not significantly altered. Scattered Epithelium in the surrounding tissue.	Prominent endothelium, no hemorrhage	No	Some eosinophils in dense area, macrophages, pneumocytes, lymphocytes and granulocytes, no karyorrhexis.	No	No
#102	MeV-S	minimal; only smallest foci, bronchial associated	Regular	Prominent endothelium, no hemorrhage	No	Some eosinophils in dense area, macrophages, pneumocytes, lymphocytes and granulocytes, no karyorrhexis.	No	Suspected

Animal-No.	Vaccine group	% Dense Area	Bronchia	Vessels	DIC	Dense Area	Fibrosis	Syncitia
#114	MeV-S	30% dense areas, bronchial associated	Bronchitis, lymphocytes and a few granulocytes in the lumen; inflammatory infiltration of the epithelium. Epithelium in the surrounding tissue.	Prominent endothelium, perivasculitis with some eosinophils, hemorrhage in the surrounding area.	No	Macrophages, pneumocytes, lymphocytes. Hardly any granulocytes and eosinophils. Sporadic karyorrhexis.	No	No
#94	Alum+S / Dexa	10% dense areas, not bronchial associated	Bronchitis, epithelium with inflammatory infiltration	Vasculitis, prominent endothelium, low inflammatory infiltration of the vessel walls	No	Some eosinophils especially around vessels (poorly visible due to hemorrhages) Macrophages, pneumocytes, lymphocytes and granulocytes.	No	No
#97	Alum+S	50% dense areas, not bronchial associated	Bronchitis, epithelium with inflammatory infiltration, granulocytes and lymphocytes in the lumen, bronchial epithelium in the surrounding tissue	Marked vasculitis with inflammatory infiltration of the wall (incl. eosinophils), many eosinophils in the surrounding of the vessel walls	No	Many eosinophils especially around vessels. Macrophages, pneumocytes, lymphocytes and granulocytes.	No	No
#101	Alum+S	50% dense areas, not bronchial associated	Epithelium not infiltrated by inflammation, blood in the lumen	Marked vasculitis with inflammatory infiltration of the vessel wall, no edema around vessels, massive hemorrhage in the surrounding tissue.	No	Massive foci of eosinophils (vessels?), macrophages, pneumocytes, lymphocytes and granulocytes.	No	No
#104	Alum+S	60% dense areas, not bronchial associated	Epithelium little affected; granulocytes in the lumen	Marked vasculitis with inflammatory infiltration of the wall.	No	Massive foci of eosinophils (vessels?), macrophages, pneumocytes, lymphocytes and granulocytes.	No	No
#106	Alum+S	70% dense areas, not bronchial associated	Bronchitis, epithelium with little inflammatory infiltration, epithelium irregular, granulocytes (eosinophils) in the lumen	Marked vasculitis with low infiltration of eosinophils in the vessel wall, massive hemorrhage in the surrounding tissue.	No	Many eosinophils especially around vessels. Macrophages, pneumocytes, lymphocytes and granulocytes. Karyorrhexis.	No	No
#107	Alum+S / Dexa	30% dense areas, not bronchial associated	Bronchitis, epithelium with little inflammatory infiltration, epithelium irregular, granulocytes (eosinophils) in the lumen	Marked vasculitis with inflammatory infiltration of the vessel wall, hemorrhage in the surrounding area.	No	Some eosinophils, but more granulocytes, macrophages, pneumocytes, lymphocytes.	No	No
#111	Alum+S / Dexa	20% dense areas, bronchial associated	Epithelium hardly affected, single eosinophils in lumen	Prominent endothelium, hemorrhages.	No	Mild Infektion, Eosinophils present, often focal, Macrophages, pneumocytes, lymphocytes, granulocytes, karyorrhexis.	No	No
#112	Alum+S	60% dense areas, not bronchial-associated, highly condensed	Epithelium hardly affected, Detritus and granulocytes in the lumen	Prominent endothelium, sporadic inflammatory inflammation in the vessel wall, massive perivascular lymphatic infiltration.	No	Some eosinophils, granulocytes, macrophages, pneumocytes, lymphocytes low karyorrhexis.	No	No

Animal-No.	Vaccine group	% Dense Area	Bronchia	Vessels	DIC	Dense Area	Fibrosis	Syncitia
#116	Alum+S / Dexa	minimal; only smallest foci, strictly bronchial associated	Regular	Prominent endothelium, sporadic inflammatory infiltration.	No	Eosinophils clearly present, macrophages, pneumocytes, lymphocytes.	No	No
#117	Alum+S / Dexa	20% dense areas, not clearly bronchial associated	Epithelium appears disorganized; no infiltration of epithelium	Prominent endothelium, vessel wall infiltrated with eosinophils. Massive eosinophils in lumen + surrounding tissues.	No	Many eosinophils, macrophages, pneumocytes, lymphocytes, granulocytes.	No	No
#118	Alum+S	70% dense areas, not bronchial associated, highly condensed	Epithelium appears disorganized; no infiltration of epithelium low amount of inflammatory cell in the lumen	Prominent endothelium massive lymphatic sheath, massive eosinophils in the lumen + around the vessels, hemorrhages.	No	Massive eosinophils present, macrophages, pneumocytes, lymphocytes, granulocytes.	No	No
#120	Alum+S / Dexa	40% dense areas, not bronchial associated	Epithelium clearly altered; occasional inflammatory infiltration, granulocytes in the lumen; epithelium in the surrounding tissue	Prominent endothelium, inflammatory infiltration (eosinophils) of the wall, no hemorrhage.	No	Some eosinophils, granulocytes, macrophages, pneumocytes, lymphocytes low karyorrhexis.	No	Suspected
hamster #1	naive	Regular	Regular	Regular.	No	Regular.	No	No
hamster #2	naive	Regular	Regular	Regular.	No	Regular.	No	No

Table S3. Statistical evaluation of selected scRNA-Seq data sets. Related to Figure 6. scRNA data concerning relevant selectively up-regulated gene sets in depicted annotared cell types between differently vaccinated hamster cohorts were analysed to reveal statistical significance of de-regulated genes as depicted in Fig. 6D and 6F. Differential expression of the selected cytokines in different celltype compartments between treatment groups was performed using the FindMarkers function from Seurat with the default parameters. *, p<0.05; **, p<0.01; ***, p<0.001; ****, p<0.0001. MΦ, macrophages; DC, dendritic cells; NK, natural killer cells; ILC, innate lymphoid cells.

all cells	*Il4*			*Il5*			*IL13*			*IL19*			*CCL11*		
	Alum+S vs. Mock	Alum+S vs. MeV	MeV vs. Mock	Alum+S vs. Mock	Alum+S vs. MeV	MeV vs. Mock	Alum+S vs. Mock	Alum+S vs. MeV	MeV vs. Mock	Alum+S vs. Mock	Alum+S vs. MeV	MeV vs. Mock	Alum+S vs. Mock	Alum+S vs. MeV	MeV vs. Mock
AT1/AT2															
Endothelial cells															
B cells															
Alveolar MΦ															
Lung MΦ										****	****		****	****	
Monocytic MΦ											*		***	****	
Treml4^{+} MΦ															
Neutrophils															
T/NK cells	*	****	***	****	****	****	****	****	***						
Myeloid DCs															
Plasmacytoid DC															
Fibroblasts															

T/NK cell compartment	*Il4*			*Il5*			*IL13*		
	Alum+S vs. Mock	Alum+S vs. MeV	MeV vs. Mock	Alum+S vs. Mock	Alum+S vs. MeV	MeV vs. Mock	Alum+S vs. Mock	Alum+S vs. MeV	MeV vs. Mock
Naive									
Memory									
Activated		****	*	**	****	****	****	****	**
Regulatory									
NK									
ILC					***			**	

Table S4. Primer and Probe sets used. 6-Carboxyfluorescein (6FAM), BlackBerry® Quencher (BBQ), Cyanine 5 (Cy5).

Name	Sequenz	Reference
E_Sarbeco_F	5´-ACAggTACgTTAATAgTTAATAgCgT-3´	Corman et al., 2020
E_Sarbeco_R	5´-ATATTgCAgCAgTACgCACACA-3´	Corman et al., 2020
E_Sarbeco probe	5‘-(6FAM)-ACACTAgCCATCCTTACTgCgCTTCg(BBQ)-3‘	Corman et al 2020
IL-5_For	5’-gCCgTAgCCATggAgATC-3’	Mendlovic et al., 2014
IL-5 Seq Rev	5’-CgATgCACAgCTggTgCT-3’	This Paper
IL-5 probe	5’-(Cy5)-AgCTgTCCACTCACCgAGCTCTACTGAC (BBQ)-3`	This Paper
RPL18 F	5‘-gTTTATgAgTCgCACTAACCg-3‘	Zivcec et al., 2011
RPL18 R	5‘-TgTTCTCTCggCCAggAA-3‘	Zivcec et al., 2011
RPL18 probe	5‘-(Cy5)-TCTgTCCCTgTCCCggATgATC(BBQ)-3‘	Zivcec et al., 2011
Eotaxin forward	5’- AgAgAgCCTgAgACCAACAC-3’	Stanelle-Bertram et al., 2020
Eotaxin reverse	5’-AACTgggATAgAgCCTgggTg-3’	Stanelle-Bertram et al., 2020
Eotaxin-probe	5’-(6FAM)-TTgTggCCACTgCCTTCACCTC (BBQ)-3’	This Paper
IL-4-F	5'-ACAgAAAAAgggACACCATgCA-3'	Espitia et al., 2010
IL-4-R	5'-gAAgCCCTgCAgATgAggTCT-3'	Espitia et al., 2010
IL-4 probe	5'-(6FAM)-AgACgCCCTTTCAgCAAggAAgAACTCC-(BBQ)-3'	Espitia et al., 2010
IL-13-F	5'-AAATggCgggTTCTgTgC-3'	Espitia et al., 2010
IL-13-R	5'-AATATCCTCTgggTCTTgTAgATgg-3'	Espitia et al., 2010
IL-13 probe	5'-(Cy5)-TggATTCCCTgACCAACATCTCTAgTTgC (BBQ)-3'	Espitia et al., 2010